Two-Dimensional Impulsively Stimulated Resonant Raman Spectroscopy of Molecular Excited States

Giuseppe Fumero,[1,2,‡] Christoph Schnedermann,[3,4,‡] Giovanni Batignani,[1] Torsten Wende,[3] Matz Liebel,[3,5] Giovanni Bassolino,[3] Carino Ferrante,[1,6] Shaul Mukamel,[7] Philipp Kukura,[3,*] and Tullio Scopigno[1,6,†]

[1]*Dipartimento di Fisica, Sapienza Universitá di Roma, Piazzale Aldo Moro 5, Roma, I-00185, Italy*
[2]*Dipartimento di Scienze di Base e Applicate per l'Ingegneria, Sapienza Universitá di Roma, Via Antonio Scarpa 14/16, Roma, I-00161, Italy*
[3]*Physical and Theoretical Chemistry Laboratory, South Parks Road, Oxford, OX1 3QZ, United Kingdom*
[4]*Cavendish Laboratory, University of Cambridge, J. J. Thomson Avenue, Cambridge CB3 0HE, United Kingdom*
[5]*ICFO -Institut de Ciencies Fotoniques, The Barcelona Institute of Science and Technology, Barcelona, 08860 Castelldefels, Spain*
[6]*Istituto Italiano di Tecnologia, Center for Life Nano Science @Sapienza, Roma, I-00161, Italy*
[7]*Department of Chemistry and Physics and Astronomy, University of California, Irvine, California 92697, USA*

(Received 26 January 2019; revised manuscript received 19 October 2019; accepted 3 December 2019; published 28 February 2020)

Monitoring the interactions between electronic and vibrational degrees of freedom in molecules is critical to our understanding of their structural dynamics. This is typically hampered by the lack of spectroscopic probes able to detect different energy scales with high temporal and frequency resolution. Coherent Raman spectroscopy can combine the capabilities of multidimensional spectroscopy with structural sensitivity at ultrafast timescales. Here, we develop a three-color-based 2D impulsive stimulated Raman technique that can selectively probe vibrational mode couplings between different active sites in molecules by taking advantage of resonance Raman enhancement. Three temporally delayed pulses generate nuclear wave packets whose evolution reports on the underlying potential energy surface, which we decipher using a diagrammatic approach enabling us to assign the origin of the spectroscopic signatures. We benchmark the method by revealing vibronic couplings in the ultrafast dynamics following photoexcitation of the green fluorescent protein.

DOI: 10.1103/PhysRevX.10.011051

Subject Areas: Atomic and Molecular Physics, Optics, Physical Chemistry

I. INTRODUCTION

The investigation of light-induced processes is essential to the understanding of a variety of complex phenomena at the interface between physics, chemistry, and biology, in which excited-state dynamics cause the transient reconfiguration of atomic positions and electronic phases. Following the absorption of a photon, the behavior of the system is dictated by the interplay between vibrational and electronic degrees of freedom of the system and the environment [1–4]. The evolution typically occurs along a multidimensional landscape, which is effectively represented by vibrationally structured potential energy surfaces (PESs) and determines the competition between all the available radiative and nonradiative relaxation channels.

Ultrafast spectroscopy exploits tailored sequences of laser pulses to photoexcite and subsequently probe these channels, with the aim of unveiling the dynamics and the underlying vibronic structure. This goal requires the correct identification of the excited-state PESs involved in the photoinduced process as well as the mapping of their relative orientations and displacements. A number of different pulse schemes and strategies have been developed to meet these tasks, but the unambiguous identification of vibronic properties, such as quasiparticle couplings, mode-mixing and nonadiabatic effects, remains challenging [5,6]—in particular, on electronically excited states after the system has left the Franck-Condon (FC) region—due to overlapping signal contributions arising from

*philipp.kukura@chem.ox.ac.uk
†tullio.scopigno@uniroma1.it
‡These authors contributed equally.

different physical processes. Linear vibrational techniques, such as infrared and spontaneous Raman spectroscopy, cannot monitor vibrational coherences on the excited states, whereas UV-visible absorption spectroscopy usually lacks the desired structural sensitivity. Considerable efforts have been aimed at the development of multidimensional spectroscopic techniques in order to separate the photoinduced response over additional spectral dimensions [7–19], which arise from the parameters tunable during the experiment, such as the time delays between multiple excitation pulses. The correlations of features on different dimensions offer a different perspective on the vibrational landscape, providing a connection between the structure of the system and its dynamics.

Coherent multidimensional Raman spectroscopy is well suited to directly address excited-state vibrational properties in time and frequency domains due to its "fingerprint" specificity over the full vibrational manifold of interest [20–24]. Furthermore, Raman spectroscopy benefits from resonance enhancements of specific chromophore signatures and thereby provides a route to comprehensively investigate vibrational energy flow during reactive transformations by selectively probing specific environments [25]. In particular, time-domain impulsive stimulated Raman scattering (ISRS) [26–36] offers several advantages over its frequency-domain analogues for the detection of vibronic features, especially for low-frequency modes, by efficiently removing elastic scattering contributions and background noise [37–40]. Its multidimensional extension, 2D-ISRS, has been theoretically proposed initially [41] and realized in both nonresonant [42,43] and resonant [44,45] implementations to study ground-state intramolecular vibrational anharmonicities, nonlinear corrections to the molecular polarizability, product-reactant correlations, and solvation dynamics, up to the recent realization of single-pulse 2D spectroscopy by means of appropriately shaped light pulses [46], with possible applications theoretically suggested for the x-ray domain [47].

The development of a 2D-ISRS scheme aimed to probe electronically excited-state vibrations would disclose the conformation of excited energy landscapes, providing direct information on specific molecular properties, such as the geometrical configuration and orientations of different PESs. This information is encoded in the harmonic fifth-order Raman response, which vanishes in the off-resonant regime. Critically, resonant 2D-ISRS demands a substantial increase in complexity, regarding both the experimental layout [48] and the data interpretation, in order to establish a protocol able to disentangle the genuine excited-state contributions from ground-state features and to assign the measured 2D peaks to the corresponding molecular origin.

Here, we address these challenges by presenting resonant excited-state 2D-ISRS. In striking contrast with the time-resolved ISRS approach—which employs a photopump to create an electronically excited-state population and monitors the temporal evolution of vibrational frequencies during a photoreaction [30,32,49]-by exploiting three femtosecond pulses for stimulating Raman coherences, we induce and probe vibronic correlations on the electronically excited manifold. Building on the resonance Raman enhancement, in our realization we tune the optical wavelengths of the pulses used in 2D-ISRS in resonance with the static and transient electronic absorption transitions to isolate contributions pertaining to a targeted electronic state. Importantly, our pulse configuration additionally suppresses undesired lower-order cascade effects, which typically mask the 2D Raman features [50,51].

We decipher the complex multidimensional response by developing an analytical method to read out the properties of vibronic coupling, which allows us to map out the multidimensional PES from the intensities and locations of diagonal and off-diagonal peaks in the 2D-ISRS spectra. We subsequently apply our approach to study the wild-type green fluorescent protein (GFP) [52,53], a prototypical system used in the fluorescence bioimaging community, during its initial photoinduced relaxation process. By collecting 2D-ISRS spectra over the full vibrational fingerprint region, we project the initially induced coherences on a separate temporal dimension and then probe their correlations as they evolve out of the FC region. We rationalize our experimental results by means of a harmonic treatment of the molecular Hamiltonian, demonstrating that this simple model is able to trace the origin of the different couplings. We further illustrate how a careful design of the experimental conditions enables the observation of dark or weak vibrational modes as coupling peaks, PES displacements along normal coordinates, and signatures of harmonic mode mixing in the excited states beyond the approximation of linearly displaced potentials.

II. RESULTS

A. Three-color 2D-ISRS technique

The pulse sequence of three-color 2D-ISRS, along with an illustrative sketch of its working principle, is presented in Figs. 1(a) and 1(b), respectively. A femtosecond, frequency-tunable actinic pulse $\mathcal{E}_a$, resonant with the S_0-S_1 absorption maximum, promotes the system into an excited electronic state S_1, and it impulsively generates vibrational coherences due to its broad spectral bandwidth, provided that the pulse duration is shorter than the vibrational period [27]. Following a variable time delay T_1, a femtosecond impulsive Raman pulse $\mathcal{E}_p$, resonant with the S_1-S_n excited-state absorption, induces additional vibrational coherences on S_1. After a second variable time delay T_2, a broadband white-light continuum (WLC) probe pulse records the temporal evolution of the vibrational coherences through spectrally-resolved transient absorption. The nonlinear polarization induced by the actinic and Raman

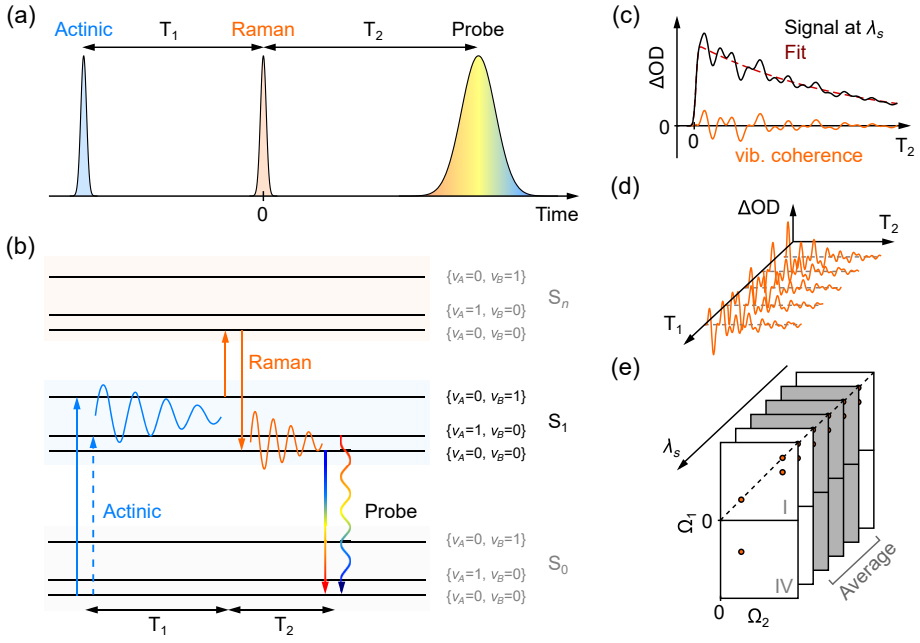

FIG. 1. Concept of 2D-ISRS. (a) Pulse sequence used for the experiment. (b) Energy ladder scheme illustrating an example of signal generation. Horizontal black lines represent the vibrational levels of the sample organized in three electronic manifolds. Dotted and solid arrows indicate light interactions with the ket and the bra side of the density matrix representing the state of the system. (c)–(e) Overview of the data analysis required in 2D-ISRS. (c) Transient absorption signals recorded along T_2 for a given T_1 over all probe wavelengths λ_s, and the vibrational coherence contribution, which is isolated by fitting and subtracting the electronic background. (d) At each λ_s, we collect the coherence for each T_1 to build $S(T_1, T_2)$, which is (e) subsequently 2D Fourier transformed to yield $S(\Omega_1, \Omega_2)$, after averaging the WLC probe wavelengths λ_s along the desired resonance region.

pulses oscillates during T_1 and T_2 at the frequencies of the stimulated Raman-active modes, thereby modulating the transmitted broadband probe pulse. The spectral content of these coherent oscillations is retrieved via a 2D Fourier transformation along T_1 and T_2, which reveals correlations between Raman modes appearing as cross and combination peaks. By tuning the actinic and Raman pulses into resonance with different excited-state transitions and selecting the probe wavelength region corresponding to the stimulated emission, the proposed scheme allows us to select S_1 as the PES on which the vibrational coherences are created and probed. We refer the reader to Fig. S2 of the Supplemental Material (SM) [54], where we report on the modification of the 2D-ISRS map upon changing the resonance condition of the probe pulse.

Specifically, we extract the oscillatory part of the detected signal at each probe wavelength along T_2 for every recorded point in time along T_1, which yields the signal $S(T_1, T_2)$ [Figs. 1(c) and 1(d)]. Note that $S(T_1, T_2)$ (reported in Fig. S1 of the SM [54]) is subsequently 2D Fourier transformed and averaged over the spectral region of interest to provide the final 2D-ISRS map $S(\Omega_1, \Omega_2)$ [Fig. 1(e); see the Appendix C for further details]. Considering that the 2D Fourier transform of a real time-domain signal is centrosymmetric, we present only the first and fourth spectral quadrants, which are associated with signal components of the same and the opposite sign along the two frequency axes, respectively [55].

Importantly, since the Raman pulse must interact with a molecule that was previously excited by the actinic pulse in order to contribute to the excited-state 2D-ISRS signal, the resonant scheme renders our technique free from lower-order background involving cascades between two different molecules that generally affect fifth-order spectroscopies [50,51,56,57].

B. Experimental measurements of wild-type GFP

To explore the capabilities of our technique, we measured resonant 2D-ISRS spectra of wild-type GFP during the early stages of its photodynamics. Under physiological conditions, the GFP chromophore exists predominantly in a neutral, protonated A_0 form [Fig. 2(a), gray structure]. Photoexcitation at about 397 nm [Fig. 2(b), gray absorption spectrum] promotes the chromophore to the first excited state A* [Fig. 2(a), blue structure], which subsequently undergoes an excited-state proton transfer (ESPT) of the phenolic proton from Tyr 66 to Glu 222, across a hydrogen bonding network to yield the highly fluorescent, deprotonated I* form [Fig. 2(a), green structure] [58].

We focus on the rapid initial (~1 ps) relaxation out of the FC region, which precedes ESPT, occurring on a longer timescale (2–10 ps) [59,60]. As the photoinduced evolution

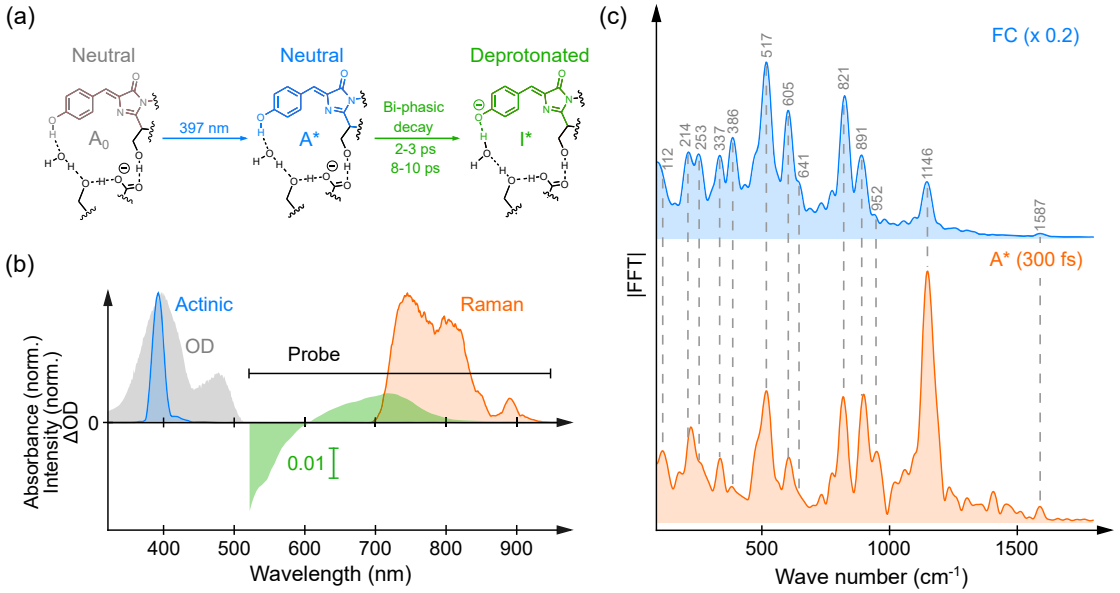

FIG. 2. Experimental characterization of wild-type GFP. (a) Photodynamics of GFP. Photoexcitation of the neutral A_0 chromophore at 397 nm prepares A*, which decays with biphasic dynamics (2–3 and 8–10 ps) to the fluorescently active deprotonated I* chromophore [59,60]. (b) Normalized absorption spectrum (gray) and transient absorption spectrum at 1 ps (green) and employed actinic and Raman pulse spectra (blue and orange). (c) Comparison of FC spectrum (blue) and A* Fourier amplitude spectrum binned in T_1 to 300 fs to average out any effect of oscillatory modulations along T_1 (orange). The absolute amplitude of the FC spectrum was scaled by 0.2 for clarity. Raman spectra were averaged over a probe wavelength region from 575 to 615 nm (stimulated emission), and coherent oscillations were Fourier transformed over a time delay of 1 ps (see Appendix C for further details).

is accompanied by a large Stokes shift, the transient absorption spectrum after 1 ps from photoexcitation at 397 nm exhibits the characteristic stimulated emission band at 509 nm known for GFP, along with a broad photoinduced absorption band at higher wavelengths [720 nm, Fig. 2(b), green spectrum]. Beyond transient absorption, we perform 1D- and 2D-ISRS measurements on GFP using a 15-fs actinic pulse in combination with a 9-fs Raman pump pulse, whose spectral envelopes are shown in Fig. 2(b) (blue and orange spectra), by following the resonant strategy described previously and sampling delays of 1 ps along the T_1 and T_2 dimensions. In Fig. 2(c), we compare the 1D spectra obtained by two-pulse ISRS in the absence of the Raman pulse, probed immediately after the photoexcitation [Fig. 2(c), blue spectrum] and after relaxation from the FC region [Fig. 2(c), orange spectrum, averaged over 300 fs along T_1], which correspond to the A* excited-state Raman spectrum. The comparison shows that the "fingerprint" Raman band positions up to 1200 cm^{-1} are not affected by the FC relaxation on A*. This observation is in line with previous observations suggesting that the proton motion leading to the formation of the I* form is not dominant in the GFP subpicosecond transient dynamics [61].

As a consequence of the negligible changes in the chromophore configuration during the initial relaxation process, the corresponding 2D-ISRS spectrum, shown in Fig. 3(a), presents pronounced peaks along the principal diagonal at $\Omega_1 = \Omega_2$ [Fig. 3(a), black dashed diagonal line] that match frequencies obtained in the corresponding excited-state A* Raman spectrum [compare to Fig. 2(c), orange spectrum]. In addition, we observe several prominent off-diagonal peaks that occur only along vertical lines [i.e., parallel to Ω_1, black dotted vertical lines in Fig. 3(a)], while horizontal correlations (parallel to Ω_2) appear to be missing. Off-diagonal peaks are gathered mainly in three regions: a vertical stripe for $\Omega_2 = 1147$ cm^{-1} and two subdiagonals for $\Omega_1 = \Omega_2 - 1010$ cm^{-1} [Fig. 3(a), red arrow] and $\Omega_1 = \Omega_2 - 2294$ cm^{-1} [Fig. 3(a), blue arrow]. The spectral separation between the ground-state absorption, stimulated emission, and excited-state absorption guarantees the absence of ground-state contamination to the excited-state 2D maps. This result is further confirmed by the lack of contributions of ground-state Raman frequencies in the measured 2D spectra.

C. Origin of the 2D-ISRS couplings within a harmonic model

The interpretation of 2D spectra is generally hampered by similar spectral features that may arise from different and concurring physical processes [62]. In order to extract the structural information contained in these measurements, we derive the 2D-ISRS signal using a perturbative framework based on the density matrix expansion [63]. We then use the obtained analytical expression (see Eq. (D1) in the Appendix) to fit the experimental data, as shown in Fig. 3(b). Further details on the signal derivation are

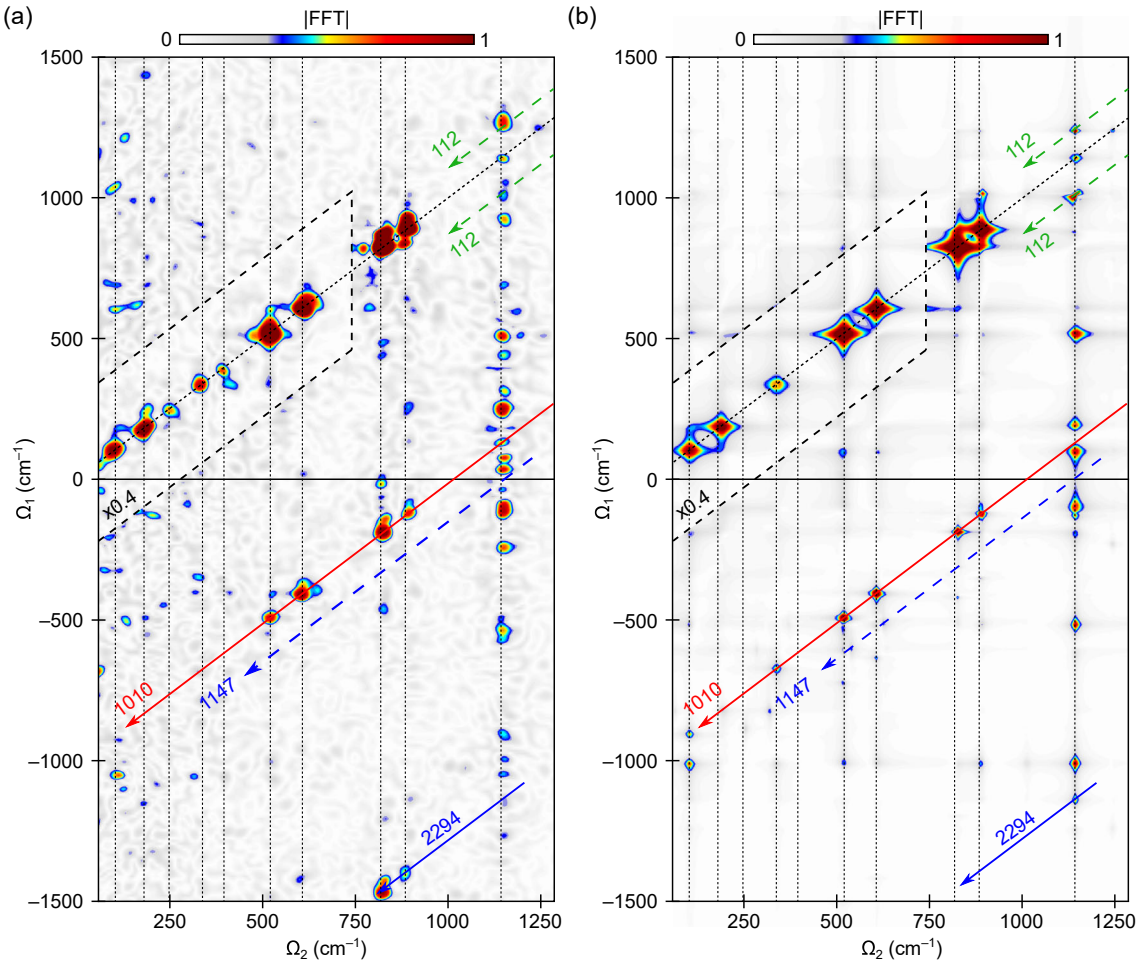

FIG. 3. The 2D-ISRS characterization of the first excited electronic state of GFP. (a) Experimental 2D-ISRS map and (b) fit to the linearly displaced harmonic model. Vertical dotted lines correspond to frequencies of the GFP excited-state vibrations, extracted by fitting the principal diagonal. The blue dashed and blue solid arrows highlight combination bands involving the fundamental and overtone frequencies of the 1147-cm^{-1} mode, respectively. As evidenced by the experimental map in panel (a), several couplings with the overtone are present, while there are no peaks on the blue dashed arrow. The red arrow highlights combination bands involving the mode at 1010 cm^{-1} that is absent along the principal diagonal. The green dashed arrow highlights a combination band between the 1147- and 112-cm^{-1} modes. The dashed area around the principal diagonal has been scaled by 0.4 for visual purposes.

presented in the Appendix D, and in Secs. c and d of the SM [54]. Briefly, the physical observables can be related to the nth order nonlinear optical polarization $P^{(n)}$, which consists of the convolution between matter correlation functions and the electromagnetic fields [63]. The radiation-matter interaction is treated perturbatively, and the density matrix is expanded in power of the fields, applying many-body Green function techniques in Liouville space. Diagrammatic representations are exploited to isolate all the relevant terms in the expansion and calculate nonequilibrium expectation values of the correlation functions [64,65]. In particular, 2D-ISRS signals originating from the fifth-order nonlinear polarization $P^{(5)}$ are represented by the Feynman diagrams shown in Fig. 4(a).

The 2D-ISRS signal depends parametrically on the frequencies ω_i and lifetimes γ_i of the modes and the dipole matrix elements μ_{ij}, in a way determined by the choice of the model molecular Hamiltonian, H_0. As H_0 is selected, these parameters can be quantitatively computed by fitting the experimental observations to the chosen model. To describe the experimental data, we assume the harmonic oscillator (HO) approximation for H_0, in which the vibrational manifold associated with each electronic state can be depicted as an n-dimensional parabola. The dipole matrix elements are given by the FC overlap integrals between the initial and final wave functions, whose PESs are displaced along the normal mode coordinates with respect to each other. It is worth stressing that deviations from the harmonic regime manifest themselves mainly in off-resonance conditions, when the harmonic contribution vanishes, allowing us to pinpoint the otherwise smaller contribution of single-mode and multimode anharmonicities and polarizability nonlinearities [42]. Conversely, under resonant conditions, the harmonic response is dominant.

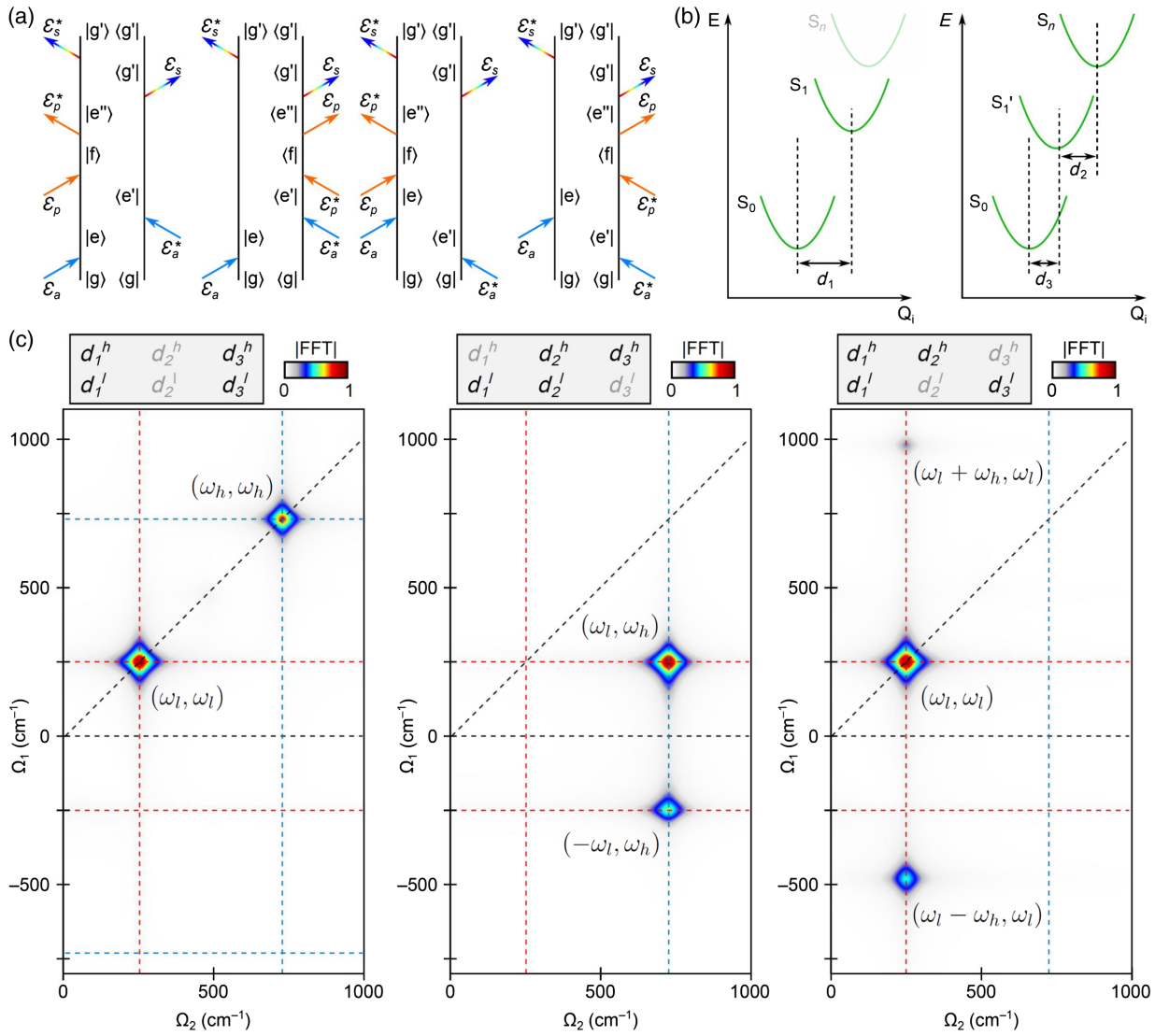

FIG. 4. Theoretical interpretation of 2D-ISRS signals in the harmonic model. (a) Double-sided Feynman diagrams describing the contributions to the signal. (b) Different energy landscapes along the vibrational coordinate Q_i probed by the actinic pulse (left panel) and Raman and probe pair (right panel). In the harmonic model, even if three electronic energy potentials are involved, three different displacements among them have to be considered, since d_1 can be different from d_3, due to the relaxation of the molecule out of the FC region. (c) Simulation of the linearly displaced harmonic model for a two-mode system $\omega_h = 730$ cm^{-1} and $\omega_l = 250$ cm^{-1} considering three different choices of the displacement set, in which two of the six parameters are set equal to zero. For each panel, the two nondisplaced coordinates are indicated in gray by the color scheme on top. The left panel shows diagonal peaks obtained for d_2^h, $d_2^l = 0$ and the other parameters different from zero; the central panel shows two cross peaks at $\Omega_1 = \pm\omega_l$, $\Omega_2 = \omega_h$ obtained by switching off d_1^h and d_3^l; in the right panel, the only vanishing displacements are d_2^l and d_3^h, which lead to a diagonal peak at ω_l and two combination bands at $\Omega_1 = \omega_h \pm \omega_l$ and $\Omega_2 = \omega_l$. Red (blue) horizontal and vertical lines highlight the ω_l (ω_h) frequency.

To connect the structural information with the 2D-ISRS maps, we first consider a linearly displaced harmonic oscillator (LDHO) model with two vibrational modes ω_l and ω_h and three electronic manifolds. Within this minimal scenario, two displacements per vibrational mode are required to determine the 2D-ISRS signal. The effect of each displacement d_i along the mode ω_i is to enhance or suppress a given component of the FC progression relative to that mode, gradually shifting the maximum from the $0 \rightarrow 0$ transition to higher overtones. Thus, the signal depends on the four displacements between the electronic surfaces along each vibrational coordinate $d_1^{h,l}$ and $d_2^{h,l}$. The displacement d_1 determines the probability of a transition to a specific vibrational state after the interaction with the actinic or the probe pulse since the two laser fields are resonant with the same electronic transition S_0-S_1. We remark that the fifth-order signal is emitted as a result of a six-wave mixing process upon an additional light-matter interaction (usually called free induction decay), which is due to the relaxation of the nonequilibrium polarization

created by the external pulses. Despite the different nature of the two interactions involving the probe-pulse modes, shown as rainbow-colored arrows in Fig. 4(a), the dipole moment associated with the free induction decay is still governed by d_1, which gives the probability for a relaxation to a specific vibrational level of the electronically ground state. Similarly, d_2 controls the probability of a transition to a determined state mediated by the Raman pulse, involving the different electronic resonance S_n-S_1. From the expressions of the FC integrals, we can determine the role of each parameter: $d_1^i \neq 0$ implies FC activity of mode i, which can be excited by the actinic pulse and probed by the WLC as a diagonal peak in the map. In order to observe combination peaks, both d_1 and d_2 of the involved modes must be finite.

In real systems, excited-state dynamics often modify this simple scenario, even in the case of the LDHO picture. For example, in the presence of a dynamic shift of the vibrational frequencies due to coupling to a thermal bath, peaks are asymmetrically broadened with respect to the principal diagonal [44,66]. Here, we consider a different situation in which the dynamics are exhausted within the finite duration of the femtosecond pulses. In this case, the displacements recorded by the actinic pulse are different from those recorded by the probe pulse, as shown by Fig. 4(b), and three displacements per mode are required to appropriately describe the 2D-ISRS spectra. For these reasons, 2D-ISRS is able to also access dynamics that are too fast to be resolved as a shift in the Raman peaks or that do not modify the frequencies of the modes but only the transition dipole moments. A common situation is that upon photoexcitation by the actinic pulse, the system evolves to a different region of the S_1 PES, and the harmonic potential describing the PES near the new minimum is shifted from the initial value corresponding to S_1^{FC} to a new value corresponding to a potential S_1', which we refer to as the dynamic LDHO. We thus described the subpicosecond dynamics of GFP through the dynamic shift of the S_1 potential induced by the actinic pulse, in line with the observed Stokes shift [see Fig. 2(b)], and we fitted the experimental data with the dynamic LDHO model [Fig. 3(b)]. Notably, at odds with the simple picture for the static two-mode LDHO described above, off-diagonal peaks are possible even if d_1 or d_3 is vanishing for one of the modes. This case is shown in Fig. 4(c), in which we present the simulated 2D-ISRS signal of the dynamic LDHO depending on three displacements for the three typical contributions that may appear in the 2D maps: diagonal peaks (ω_i, ω_i), cross peaks (ω_i, ω_j), and combination peaks $(\omega_i \pm \omega_j, \omega_i)$. The corresponding dominant Liouville pathways are reported in Sec. e of the SM [54]. Specifically, setting two of the six available parameters equal to zero, it is possible to understand the effect of each displacement. A vanishing d_2 along both the vibrational cordinates results in diagonal peaks at the two vibrational frequencies ω_l and ω_h [Fig. 4(c), left panel]. Cross peaks between the two modes arise from switching off d_1 for one mode and d_3 for the other. For example, the cross peaks at $\Omega_1 = \pm\omega_l$, $\Omega_2 = \omega_h$ in the central panel of Fig. 4(c) can be obtained with $d_1^h = 0$ and $d_3^l = 0$. Finally, combination bands at $\Omega_1 = \omega_h \pm \omega_l = \omega_\pm$ and $\Omega_2 = \omega_l$ as shown in the right panel of Fig. 4(c) are isolated by setting d_3^h and d_2^l equal to zero.

Building on such considerations based on the dynamic LDHO model, we can summarize the conditions that generate the different contributions in the 2D-ISRS maps:

(i) A diagonal peak at (ω_i, ω_i) results from $d_1^i, d_3^i \neq 0$.
(ii) A cross peak at $(\pm\omega_i, \omega_j)$ indicates that d_2 is not vanishing, and it is comparable for the two modes.
(iii) A combination peak at $(\omega_i \pm \omega_j, \omega_i)$ implies a nonvanishing and comparable d_1 for the two modes. Similarly, a combination band at $(\omega_i, \omega_i \pm \omega_j)$ implies a nonvanishing and comparable d_3. Both additionally require $d_2^j \neq 0$.

In general, all these processes contribute to the total signal, with weights depending on the relative magnitude of the displacements. Since the signal emission requires the state of the density matrix after the free induction decay to be diagonal (see Sec. c of the SM [54] and Ref. [63]), an off-diagonal 2D-ISRS peak is obtained if the interaction with at least one of the pulses changes the total vibrational quantum number n by two so that $\Delta n = \sum_i |\Delta n_i| = 2$. For the cross and combination peaks analyzed above, this process is mediated by the Raman and the actinic pulses, respectively. Even if, in general, many vibrational modes are present, correlations between more than two modes are negligible in the limit of small displacements because they involve multiple higher-order processes with $\Delta n > 1$. Thus, the scheme we built for the two-mode LDHO can be applied to multimode systems by considering all possible pairs.

Finally, we note that, by exploring more than two different electronic surfaces, resonant 2D-ISRS is sensitive to the sign of displacements, a key advantage over lower-order 1D techniques only capable of resolving their magnitude. Indeed, if only one electronic transition is probed (for instance, $S_0 \rightarrow S_1$), the signal is totally symmetric with respect to a change of the sign of d_1. This result happens because, even if transitions with an odd difference of quantum numbers in the initial and final states scale linearly with the displacement, the displacement appears squared in the signal since two transitions between the same states are required to go back to a diagonal state of the density matrix. Probing an additional excited state breaks this symmetry. Even if no change occurs when all the excited-state potentials are displaced in the same direction, a different sign between pairs of d_i and d_j will modify the spectrum. Linear and also third-order techniques usually probe resonances between two electronic states, while resonant 2D-ISRS is able to specifically probe three PESs at the same time.

III. DISCUSSION

Building on the results of the LDHO model, we can now interpret the 2D-ISRS signal of GFP. The peaks shown in the experimental map and retrieved by the theoretical

simulation (Fig. 3) can be classified according to the three families of diagonal, combination, and cross peaks presented in the previous section. For example, we interpret the feature at ($\Omega_1 = -424$ cm^{-1}, $\Omega_2 = 822$ cm^{-1}) as a combination band between the 822 and 1248 cm^{-1} modes, indicating that d_1^{1248}, d_1^{822}, and $d_2^{1248} \neq 0$. Here, we discuss the implications of the predominant features in the 2D map, while we refer to Sec. f of the SM [54] for a table summarizing the origin of all the diagonal and off-diagonal bands obtained by the fit. The presence of off-diagonal peaks along vertical and diagonal rather than horizontal lines suggests that combination peaks at ($\omega_i \pm \omega_j$, ω_i) are primarily observed and, consequently, that most of the modes are displaced along d_1 since combination bands require a nonvanishing d_1 for both of the modes involved in the signal generation. The 1010 − cm^{-1} mode shows high FC activity on the S_n state, testified by the subdiagonal at $\Omega_1 \approx \Omega_2 - 1010$ cm^{-1} (Fig. 3, red arrow), which corresponds to a series of combination bands with other peaks due to its large d_2. In contrast, the absence of any features at 1010 cm^{-1} on the principal diagonal shows that $d_3 = 0$ for this mode. These observations illustrate the capability of 2D-ISRS of uncovering dark or weak bands by boosting small FC displacements via another transition.

We further observe coupling between the 1147-cm^{-1} phenolic C-H bend and a low-frequency mode at about 112 cm^{-1} (Fig. 3, green dashed arrow), which has recently been under discussion fueled by results from femtosecond stimulated Raman measurements on GFP in both the frequency and time domain [21,61]. While the functional importance of this coupling for the ESPT is under debate, the observation of oscillatory modulation of the excited-state Raman spectrum is generally attributed to anharmonic vibrational coupling. Conversely, related studies on other molecules suggest that anharmonic couplings are challenging to isolate and interpret in fifth-order experiments due to competitive cascade processes [51]. Our study instead highlights that the coupling between the 1147- and 112-cm^{-1} modes can also be explained within a harmonic model by the displacement of the excited-state PES along these vibrational coordinates, as supported by the agreement between the combination band in our 2D measurements and fit. We further note that the intensity of this combination band is stronger above the principal diagonal than below, suggesting additional contributions due to a cross peak between the 1147-cm^{-1} and the 1248-cm^{-1} mode. Within our framework, single coupling peaks in the 2D map do not necessarily imply a functional importance for the ESPT reaction coordinate, but the determination of the displacements and PES orientations retrieved from the 2D-ISRS features allows for identifying the coordinates more involved in the relaxation during the first picosecond after the photoexcitation. In the case of GFP, this timescale involves the relaxation of the molecular structure towards the optimal geometry to support the ESPT [61]. In particular, the values of the displacements for the mode at 1010 cm^{-1} point to a relaxation of the system upon photoexcitation along this normal coordinate, which is initially in an out-of-equilibrium configuration ($d_1 \neq 0$) and fully relaxed at the end ($d_3 = 0$).

Beyond the 112-cm^{-1} mode, we observe additional couplings of the C-H phenol mode at 1147 cm^{-1} (Fig. 3, vertical dotted line at 1147 cm^{-1}). According to the model discussed so far, the series of peaks along the vertical at $\Omega_2 = 1147$ cm^{-1} indicates a large value of d_1 and d_3 for this mode, while the absence of a subdiagonal at $\Omega_1 \approx \Omega_2 - 1147$ cm^{-1} points to a small value of d_2. Critically, the subdiagonal $\Omega_1 = \Omega_2 - 2294$ cm^{-1} (highlighted by the blue solid arrow in Fig. 3) is not captured by this model. Within the LDHO model, these features would indicate a strong d_2 displacement for the 1147 − cm^{-1} mode, such that both the fundamental and the overtone become FC active on the S_n state. This hypothesis is, however, at odds with the absence of any peaks for $\Omega_1 = \Omega_2 - 1147$ cm^{-1} in the measured map [Fig. 3(a), blue dashed arrow].

A possible explanation of this discrepancy is the presence of a mode mixing between high- and low-frequency modes in the excited state, arising in the presence of two electronic states that have different equilibrium geometries with nonparallel corresponding normal modes, commonly denoted as Duschinsky rotation [67–69]. Under such circumstances, the normal coordinates on the excited state (Q') can be expressed as a function of the ground state (Q) as $Q' = JQ + D$, where J is the orthogonal Duschinsky matrix which depends on the rotation angles Θ_D and D is the displacement vector. Even if the excited state is not displaced, the transition $0 \rightarrow n$ with $n \neq 0$ can be strong, if the mode is coupled by the Duschinsky rotation ($J \neq \mathbb{I}$) to a displaced one. In a similar way, the FC activity of a displaced mode can decrease due to the coupling to other modes.

In order to test this hypothesis, we evaluate the 2D-ISRS response of GFP incorporating in the model a mixing between the 1147-cm^{-1} and 80-cm^{-1} modes, with a fixed $\Theta_D = 90°$ Duschinsky angle. In particular, by fitting the experimental data considering the modes at 80, 822, 888, and 1147 cm^{-1}, which are those involved in the generation of the off-diagonal peaks at $\Omega_1 = \Omega_2 - 2294$ cm^{-1}, we are able to reproduce the experimental features missing in the LDHO model, as shown in Figs. 5(a) and 5(b). It is now worth dissecting the implications of the Duschinsky mechanism on the relative intensities between the fundamental and overtone contributions to combination bands. To this aim, we isolate the effect of Duschinsky rotation in Fig. 5 by considering the minimal scenario of a single mode (1147 cm^{-1}), coupled to a nondisplaced low-frequency mode (80 cm^{-1}), detected on a "spectator" mode (822 cm^{-1}). In the absence of any

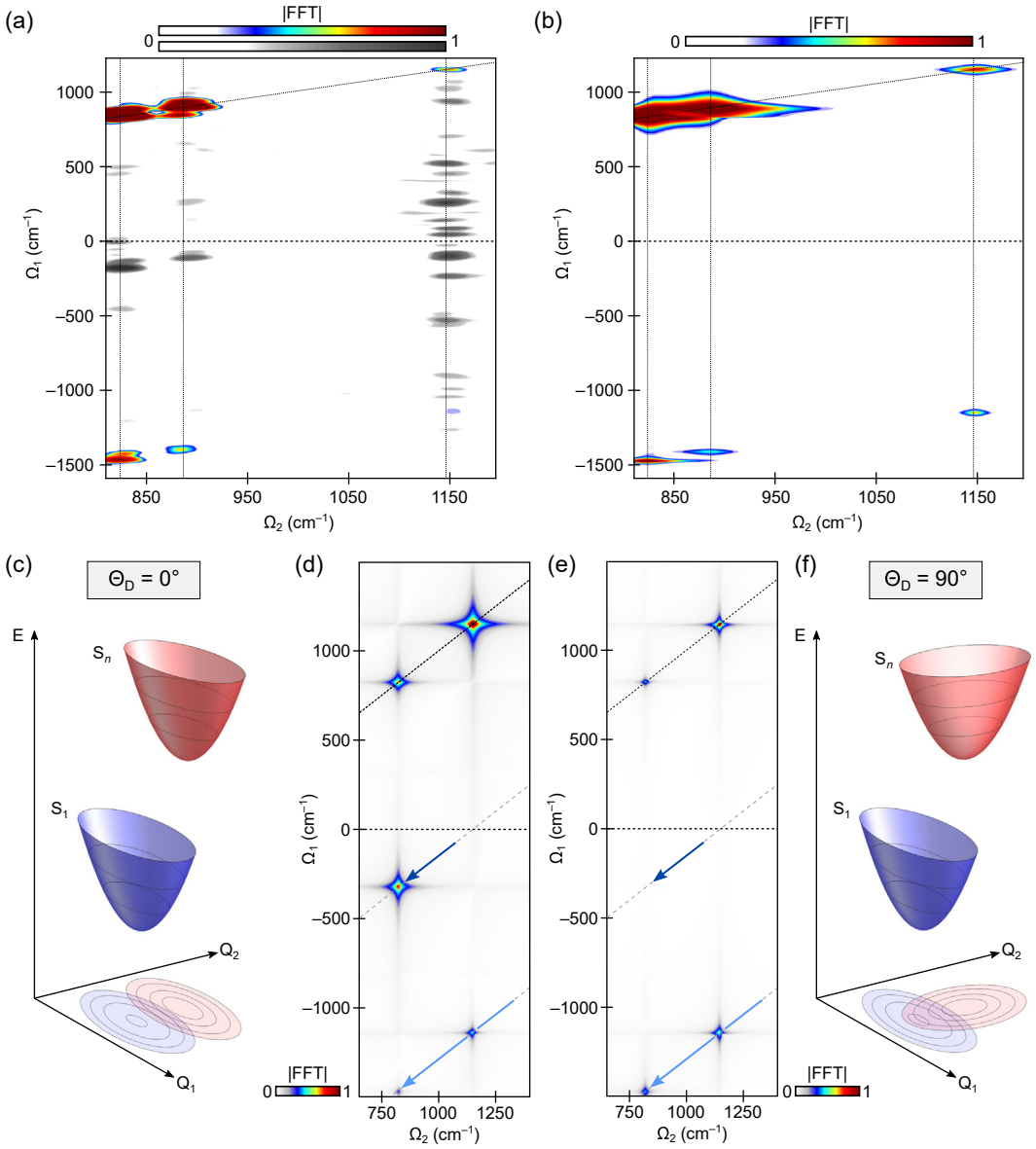

FIG. 5. Effect of mode mixing in 2D-ISRS for a harmonic model. The experimental spectra of GFP (a) are compared with the fit (b) obtained by considering the modes at 80, 822, 888, and 1147 cm^{-1}, which are those relevant for the off-diagonal peaks at $\Omega_1 = \Omega_2 - 2294$ cm^{-1}. These features, not captured by the LDHO model, are explained by a Duschinsky rotation of $\Theta_D = 90°$ between the 1147- and 80-cm^{-1} modes, and they are highlighted by the rainbow color bar in the experimental map. The gray scale has been used for the peaks not relevant for these processes and already assigned by the LDHO model. In the bottom panels, the effect of the Duschinsky rotation is dissected by considering the minimal scenario of a single mode (1147 cm^{-1}), coupled to a nondisplaced low-frequency mode (80 cm^{-1}) and detected on a "spectator" mode (822 cm^{-1}). For $\Theta_D = 0°$ (a,b), the system is described by a linearly displaced harmonic model, and a displacement $d_2^{1147} \neq 0$ causes the combination bands involving this mode and its overtones. The blue and cyan arrows indicate the position of combination bands associated with 1147 cm^{-1} and 2×1147 cm^{-1}, respectively. (c,d) In the presence of a Duschinsky rotation $\Theta_D = 90°$ between the projections of S_1 and S_n along the normal coordinates of the 1147- and 80-cm^{-1} modes, the combination band associated with the fundamental of the 1147 cm^{-1} is suppressed.

mixing, i.e., for a vanishing Duschinsky angle $\Theta_D = 0$, $d_2^{1147} \neq 0$ is needed to observe coupling with the overtone of the 1147-cm^{-1} mode, leading to the two subdiagonals at $\Omega_1 = \Omega_2 - 1147$ cm^{-1} and $\Omega_1 = \Omega_2 - 2294$ cm^{-1} [Figs. 5(c) and 5(d), blue and cyan arrows, respectively]. Conversely, a rotation of $\Theta_D \neq 0°$ between projections of the excited states S_1 and S_n along the 1147- and 80-cm^{-1} modes leads to a suppression of the subdiagonal peak at the fundamental frequency $\Omega_1 = \Omega_2 - 1147$ cm^{-1} and enhances the intensity of the overtone couplings [Figs. 5(e) and 5(f)]. The suppression is maximized at $\Theta_D = 90°$ for these values of the parameters and is above

65% for all the values of Θ_D in the range 65°–115° (see Fig. S4 of the SM [54]).

We note that the correct identification of the origin of all the off-diagonal peaks—and, in particular, the assignment of peaks involving the overtone of the 1147 cm^{-1}—is required to prevent wrong interpretations of the spectra; more importantly, it demonstrates the sensitivity of this technique to the Duschinsky mixing. Since the Duschinsky rotation affects the relative weights between vibronic transitions, mode mixing has a large impact on the kinetics and efficiency of charge transfer processes [70–72], making 2D-ISRS particularly suitable for studying this class of samples.

IV. CONCLUSIONS

We introduced a resonant 2D-ISRS technique for multidimensional Raman spectroscopy. By implementing a three-color experimental scheme, we demonstrated how to decipher the correlation between vibronic modes in electronically excited molecules with electronic-state selectivity, using a perturbative sum-over-states approach. Specifically, we showed that resonant 2D-ISRS is sensitive to such correlations also in the absence of anharmonicities and efficiently suppresses lower-order cascade signals, which affect other fifth-order Raman techniques. Moreover, using a WLC probe enabled us to further isolate the electronic states from which 2D-ISRS features originate, allowing us to study the vibrational manifolds on electronically excited states. Upon identifying the vibronic origin of each peak in 2D-ISRS maps, we elucidated how different mechanisms such as linear displacements along specific normal coordinates and mode mixing contribute to the experimental signal. Notably, while lower-order techniques can only record one-dimensional projections of potential energy surfaces, 2D-ISRS is able to efficiently map complex PESs, determining FC overlaps directly over multiple dimensions.

As a proof of concept for the experimental scheme and theoretical model, we applied the technique to study the subpicosecond FC relaxation in GFP. We revealed that high-frequency mode correlations can be sustained even by fully harmonic interactions and showed that the model is capable of reproducing the previously observed coupling of the 112- and 1147-cm^{-1} modes. In particular, we found large FC activity on the excited state of a mode that is dark in the stimulated emission transitions and an enhancement of the mode overtones, which we linked to the presence of Duschinsky mixing. In the presence of ultrafast dynamics on the electronically excited state, the selectivity of 2D-ISRS can be exploited to directly access the structural conformation on the state in which the dynamics originate, disclosing the initial stages of the reaction. We anticipate that comparing mode displacements between electronic states involved for the reactant and product may be relevant to identify the key reaction coordinates implied at different stages of the photodynamics.

ACKNOWLEDGMENTS

C. S. acknowledges financial support by the Royal Commission for the Exhibition of 1851. G. Bat. acknowledges the "Avvio Alla Ricerca 2018" grant by Sapienza Universitá di Roma. T. W. acknowledges the Marie Curie Intra-European Fellowship (PIEF-GA-2013-623651) within the 7th European Community Framework Programme. S. M. gratefully acknowledges the support of the National Science Foundation Grant No. CHE-1663822.

APPENDIX A: SAMPLE PREPARATION

Plasmids containing wild-type GFP were transformed in an *E. coli* BL21(DE3) cell line [73]. Briefly, 0.5 μl of plasmid were added in 25 μl of competent BL21(DE3) cells and incubated on ice for 25 min, heat shocked for 45 s at 42 °C, and incubated further for 2 min on ice, followed by the addition of 150 μl of prewarmed at 37 °C super optimal broth with catabolite repression media and incubation at 37 °C with shaking for one hour. In a Lysogeny broth (LB)-media Petri dish supplemented with 100 μg/mL kanamycin, 50 μl of the cell culture were plated and incubated overnight at 37 °C. A few colonies were selected and allowed to inoculate 100 μl of LB media in the presence of 100 μg/mL of the appropriate antibiotic and allowed to grow overnight.

The overnight cell culture was used to inoculate 8 L (1×8 L in 2-L flasks) of LB media with 100 μg/ml antibiotic. Cells were grown at 37 °C to an OD_{600} of 0.6–0.8 upon which 0.5 mM IPTG was added. GFP was expressed overnight at 20 °C. Cells were harvested through centrifugation at 10 000 xg for 10 min, and the pellets were resuspended in cell lysis buffer (300 mM NaCl, 50 mM Tris, pH 7.4) supplemented with a protease inhibitor tablet (Roche). Cells were lysed by microfluidizer, and the cell debris were removed by centrifugation at 20 000 xg for 20 min. In the supernatant, imidazole was added to a final concentration of 20 mM, and the first purification step was achieved by immobilized metal ion affinity chromatography (IMAC) utilizing a 20-mL IMAC column equilibrated in buffer A (300 mM NaCl, 20 mM Tris, and 20 mM imidazole, pH 7.4). After four column volume washes with buffer A, the sample was eluded with buffer B (300 mM NaCl, 20 mM Tris, and 500 mM imidazole, pH 7.4). The sample was concentrated to a final volume of 10 mL and loaded in a size exclusion chromatography (SEC) column 26/60 Superdex 75 previously equilibrated in SEC buffer (150 mM NaCl and 20 mM Tris, pH 7.4). The selected fractions were pooled and concentrated to the final $OD_{397} = 9$.

During the spectroscopy experiments, the sample (~10 ml) was continuously flowed through a 200-μm path-length flowcell at sufficient speed to ensure sample

replenishment during consecutive shots. To minimize thermal degradation, the sample reservoir was ice cooled.

APPENDIX B: EXPERIMENTAL SETUP

All pulses were derived from a Yb:KGW amplifier laser system (Pharos, Lightconversion) providing 5-W, 180-fs pulses centered at 1030 nm at a 10-kHz repetition rate. The Raman pulse [800 nm, 9 fs, 160 nJ, sample beam diameter of 55-μm full width at half maximum (FWHM)] was generated by a noncollinear optical parametric amplifier (NOPA) pumped by the second harmonic of the laser (515 nm) [74]. The pulse energy was adjusted to keep two-photon absorption of ground-state molecules below 1%. The actinic pulse (400 nm, ~15 fs, 150 nJ, sample beam diameter of 80-μm FWHM) was generated by frequency doubling the output of a second Raman NOPA (800 nm, 10 fs, 6 μJ) in a 25-μm beta-barium-borate crystal ($\theta = 29°$) placed near the sample. The fundamental was removed by two reflective harmonic separators (Eksma Optics). Probe pulses (sample beam diameter: 35-μm FWHM) were generated via WLC generation in a 3-mm sapphire crystal and detected in a home-built single-shot prism spectrograph [27]. The actinic and Raman pulses were modulated at 2.5 and 5.0 kHz by mechanical choppers, respectively, to remove lower-order contributions to the signal. T_1 and T_2 were sampled in 10.1- and 5.36-fs steps (Thorlabs–LNR50S/M and PhysikInstrumente–M-230.10, respectively). The exact step size for each translation stage was determined by reference ISRS measurements on toluene with the same pulse parameters. All pulses were vertically polarized.

APPENDIX C: DATA ANALYSIS

The data analysis is analogous to previously reported time-domain Raman studies involving an actinic and Raman pulse [30]. Briefly, for each time point along T_2, we record three wavelength-resolved transient absorption maps as a function of T_2, corresponding to the Raman-pulse-induced differential absorbance in the presence and absence of the actinic pulse as well as the actinic-pulse-induced differential absorbance in the absence of the Raman pulse. For all three transient absorption maps, we discard time delays prior to $T_2 = 100$ fs, due to cross-phase modulation [75,76], and describe the electronic background by a global fit consisting of a sum of three exponential decay functions to isolate the underlying vibrational coherence. For each probe wavelength, we subsequently construct the two-dimensional signal $S(T_1, T_2)$ and apply a 2D mono-exponentially modified Gaussian window function [23-fs rise time (sigma), 1526-fs decay constant in T_2, and 6-fs rise time (sigma), 422-fs decay constant in T_1] prior to zero padding and 2D fast Fourier transformation. To selectively probe only S_1 vibrational coherences, we only included data greater than 536 fs in T_2, thereby suppressing additional signals due to higher-lying excited electronic states. Importantly, both time delays covered a total of 1 ps to avoid possible distortions upon Fourier transformation. The final 2D-ISRS map is generated by averaging all detected probe wavelengths over the red side of the stimulated emission.

The FC spectrum [Fig. 2(c), blue] was obtained by Fourier transformation of the vibrational coherence in the absence of the Raman pulse. The A* spectrum [Fig. 2(c), orange] was generated by first subtracting the Raman-probe vibrational coherences in the absence of the actinic pulse from the vibrational coherences in its presence prior to Fourier transformation along T_2 to yield the signal $S(T_1, \Omega_2)$ and averaging over the first 300 fs along T_1. The 2D-ISRS Fourier map in Fig. 3(a) was generated by applying the same subtraction procedure for consistency. We remark, however, that the ground-state contributions do not evolve along T_1 in the absence of the actinic pulse, resulting in similar 2D-ISRS maps with and without a ground-state subtraction procedure.

APPENDIX D: SIGNAL DERIVATION

We consider, as a reference model, a three-electronic-level system with a ground state and two excited electronic states, S_0, S_1, and S_n, as depicted in Fig. 1(c), with the associated vibrational manifolds. The total field $\mathcal{E}$ acting on the sample consists in the three delayed pulses described above.

The 2D-ISRS signal is given by a convolution between the field amplitudes and the matter correlation function $\mathcal{F}$, derived from the four Feynman pathways shown in Fig. 4(a):

$$S^{(5)}(\omega, T_1, T_2) = \mathbf{Im}\left[\left(-\frac{i}{\hbar}\right)^5 \int_{-\infty}^{\infty} dt e^{i\omega t}\mathcal{E}_s^*(\omega) \int_{-\infty}^{t}\int_{-\infty}^{t_5}\int_{-\infty}^{t_4}\int_{-\infty}^{t_3}\int_{-\infty}^{t_2} dt_5 \ldots dt_1 \mathcal{E}_a(t_1)\mathcal{E}_a^*(t_2) \times \mathcal{E}_p(t_3 - T_1)\mathcal{E}_p^*(t_4 - T_1)\mathcal{E}_s(t_5 - T_2 - T_1)\mathcal{F}(t, t_1, t_2, t_3, t_4, t_5)\right].$$

Note that $\mathcal{F}$ can be expanded as a sum over states (SoS) [64] corresponding to the eigenfunctions of free molecule Hamiltonian H_0, obtaining

$$S^{(5)}(\omega,T_1,T_2)=\sum_{\substack{g,g',f,\\ e,e',e''}}K(g)\mathbf{Im}\left\{\left[\frac{\mu_{g'e''}\mu^*_{g'e'}\mathcal{E}^*_s(\omega)\mathcal{E}_s(\omega-\omega_{e''e'})}{2(\omega-\tilde{\omega}_{e''g'})}-\frac{\mu_{g'e''}\mu^*_{e'g'}\mathcal{E}_s(\omega)\mathcal{E}^*_s(\omega+\omega_{e''e'})}{2(\omega+\tilde{\omega}_{g'e'})}\right]\right.$$
$$\left.\times e^{-i\tilde{\omega}_{ee'}T_1}e^{-i\tilde{\omega}_{e''e'}T_2}\mu_{e''f}\mu^*_{fe}\mathcal{W}_p(\omega_{e''e'}-\omega_{ee'},\tilde{\omega}_{e''e'}-\tilde{\omega}_{fe'})\mu_{e'g}\mu^*_{eg}[\mathcal{W}_a(\omega_{ee'},\tilde{\omega}_{ee'}-\tilde{\omega}_{eg})-\mathcal{W}_a(\omega_{ee'},\tilde{\omega}_{ge'})]\right\}, \tag{D1}$$

where $\tilde{\omega}_{ij}=\omega_i-\omega_j-i\Gamma_{ij}$, μ_{ij} are the matrix elements of the dipole operator V, and the weighted pulse spectral densities $\mathcal{W}_k$ for $k=a,\ p$ are defined as

$$\mathcal{W}_k(\omega_1,\tilde{\omega}_2)=\int_{-\infty}^{+\infty}d\omega'\frac{\mathcal{E}_k(\omega'+\omega_1)\mathcal{E}^*_k(\omega')}{2(\omega'+\tilde{\omega}_2)} \tag{D2}$$

and rule the resonant bandwidth accessible by the finite widths of the actinic and Raman pulses. The subscripts e, e', e'' run over the vibrational levels of S_1, while f and g, g' run over those of S_n and S_0, respectively. The initial thermal population is ruled by the Boltzman factor $K(g)$ that depends on the temperature. At room temperature, vibrational modes above a few hundred wave numbers are initially populated only in the vibrational ground state; i.e., g in Eq. (D1) is fixed. The displacements d_n, $n=1,2,3$, and the Duschinsky angle Θ_D enter in the signal expression via the dipole matrix elements μ_{ij} as detailed in Sec. d of the SM [54]. Specifically, we note that the functional dependence of the signal on each displacement is the same since the signal is proportional to a product of six dipoles and each d_n appears in two of them. Finally, a Fourier transformation over the two delays and the integration on ω lead to the 2D frequency correlation map:

$$S^{(5)}(\Omega_1,\Omega_2)=\int_{-\infty}^{+\infty}d\omega\times\int_{-\infty}^{+\infty}dT_1dT_2e^{i\Omega_1T_1+i\Omega_2T_2}S^{(5)}(\omega,T_1,T_2). \tag{D3}$$

Using a WLC probe, the effective domain of integration over ω is restricted by the bandwidth of the pulse $\mathcal{E}(\omega)$. In our experimental implementation, the measurement is spectrally resolved in ω, and a selective average over a specific spectral region can be exploited to isolate the resonant contributions from the stimulated emission or the excited-state absorption of the system. In particular, here the signal has been averaged over the tail of the stimulated emission region of the GFP, from 575 to 615 nm, while the corresponding maps averaged on the excited-state absorption are presented in Fig. S2 of the SM [54].

In the SoS picture, the signal is determined by the contributions originating from different pathways in the Liouville space, which corresponds to the different permutation of the SoS indexes. In this way, the contribution of selected modes to the signal can be easily isolated, overcoming interpretative issues due to interference between different nonlinear optical effects, in addition to giving the advantage of speeding up the calculations by removing the contributions to an unobserved region of the spectrum. In the simulations, we did not include the contributions to the signal lying on one of the two axes, originating from pathways in which populations instead of coherences evolve during T_1 or T_2, since they provide the same information of third-order techniques and are suppressed by the experimental analysis routine. Further details on the signal derivation are provided in Secs. c and d of the SM [54].

[1] J. C. Polanyi and A. H. Zewail, *Direct Observation of the Transition State*, Acc. Chem. Res. **28**, 119 (1995).

[2] G. D. Scholes, G. R. Fleming, L. X. Chen, A. Aspuru-Guzik, A. Buchleitner, D. F. Coker, G. S. Engel, R. van Grondelle, A. Ishizaki, D. M. Jonas, J. S. Lundeen, J. K. McCusker, S. Mukamel, J. P. Ogilvie, A. Olaya-Castro, M. A. Ratner, F. C. Spano, K. B. Whaley, and X. Zhu, *Using Coherence to Enhance Function in Chemical and Biophysical Systems*, Nature (London) **543**, 647 (2017).

[3] F. D. Fuller, J. Pan, A. Gelzinis, V. Butkus, S. S. Senlik, D. E. Wilcox, C. F. Yocum, L. Valkunas, D. Abramavicius, and J. P. Ogilvie, *Vibronic Coherence in Oxygenic Photosynthesis*, Nat. Chem. **6**, 706 (2014).

[4] X. Gong, O. Voznyy, A. Jain, W. Liu, R. Sabatini, Z. Piontkowski, G. Walters, G. Bappi, S. Nokhrin, O. Bushuyev, M. Yuan, R. Comin, D. McCamant, S. O. Kelley, and E. H. Sargent, *Electron-Phonon Interaction in Efficient Perovskite Blue Emitters*, Nat. Mater. **17**, 550 (2018).

[5] J. Zhou, W. Yu, and A. E. Bragg, *Structural Relaxation of Photoexcited Quaterthiophenes Probed with Vibrational Specificity*, J. Phys. Chem. Lett. **6**, 3496 (2015).

[6] G. Batignani, E. Pontecorvo, C. Ferrante, M. Aschi, C. G. Elles, and T. Scopigno, *Visualizing Excited-State Dynamics of a Diaryl Thiophene: Femtosecond Stimulated Raman Scattering as a Probe of Conjugated Molecules*, J. Phys. Chem. Lett. **7**, 2981 (2016).

[7] M. Cho, *Coherent Two-Dimensional Optical Spectroscopy*, Chem. Rev. **108**, 1331 (2008).

[8] D. M. Jonas, *Two Dimensional Femtosecond Spectroscopy*, Annu. Rev. Phys. Chem. **54**, 425 (2003).

[9] P. Hamm and M. Zanni, *Concepts and Methods of 2D Infrared Spectroscopy* (Cambridge University Press, Cambridge, England, 2012).
[10] M. Fayer, *Dynamics of Liquids, Molecules, and Proteins Measured with Ultrafast 2D IR Vibrational Echo Chemical Exchange Spectroscopy*, Annu. Rev. Phys. Chem. **60**, 21 (2009).
[11] S.-H. Shim and M. T. Zanni, *How to Turn Your Pump–Probe Instrument into a Multidimensional Spectrometer: 2D IR and Vis Spectroscopies via Pulse Shaping*, Phys. Chem. Chem. Phys. **11**, 748 (2009).
[12] A. Halpin, P. J. M. Johnson, R. Tempelaar, R. S. Murphy, J. Knoester, T. L. C. Jansen, and R. J. D. Miller, *Two-Dimensional Spectroscopy of a Molecular Dimer Unveils the Effects of Vibronic Coupling on Exciton Coherences*, Nat. Chem. **6**, 196 (2014).
[13] N. H. C. Lewis and G. R. Fleming, *Two-Dimensional Electronic-Vibrational Spectroscopy of Chlorophyll a and b*, J. Phys. Chem. Lett. **7**, 831 (2016).
[14] T. L. Courtney, Z. W. Fox, K. M. Slenkamp, and M. Khalil, *Two-Dimensional Vibrational-Electronic Spectroscopy*, J. Chem. Phys. **143**, 154201 (2015).
[15] I. A. Finneran, R. Welsch, M. A. Allodi, T. F. Miller, and G. A. Blake, *Coherent Two-Dimensional Terahertz-Terahertz-Raman Spectroscopy*, Proc. Natl. Acad. Sci. U.S.A. **113**, 6857 (2016).
[16] D. B. Turner, K. W. Stone, K. Gundogdu, and K. A. Nelson, *Three-Dimensional Electronic Spectroscopy of Excitons in GaAs Quantum Wells*, J. Chem. Phys. **131**, 144510 (2009).
[17] M. Grechko, T. Hasegawa, F. D'Angelo, H. Ito, D. Turchinovich, Y. Nagata, and M. Bonn, *Coupling between Intra- and Intermolecular Motions in Liquid Water Revealed by Two-Dimensional Terahertz-Infrared-Visible Spectroscopy*, Nat. Commun. **9**, 885 (2018).
[18] A. P. Spencer, W. O. Hutson, and E. Harel, *Quantum Coherence Selective 2D Raman–2D Electronic Spectroscopy*, Nat. Commun. **8**, 14732 (2017).
[19] E. Harel, *Four-Dimensional Coherent Electronic Raman Spectroscopy*, J. Chem. Phys. **146**, 154201 (2017).
[20] T. Buckup and J. Léonard, *Multidimensional Vibrational Coherence Spectroscopy*, Top. Curr. Chem. **376**, 35 (2018).
[21] T. Fujisawa, H. Kuramochi, H. Hosoi, S. Takeuchi, and T. Tahara, *Role of Coherent Low-Frequency Motion in Excited-State Proton Transfer of Green Fluorescent Protein Studied by Time-Resolved Impulsive Stimulated Raman Spectroscopy*, J. Am. Chem. Soc. **138**, 3942 (2016).
[22] D. P. Hoffman, S. R. Ellis, and R. A. Mathies, *Characterization of a Conical Intersection in a Charge-Transfer Dimer with Two-Dimensional Time-Resolved Stimulated Raman Spectroscopy*, J. Phys. Chem. A **118**, 4955 (2014).
[23] D. T. Valley, D. P. Hoffman, and R. A. Mathies, *Reactive and Unreactive Pathways in a Photochemical Ring Opening Reaction from 2D Femtosecond Stimulated Raman*, Phys. Chem. Chem. Phys. **17**, 9231 (2015).
[24] Z. Zhang, A. Huerta-Viga, and H.-S. Tan, *Two-Dimensional Electronic-Raman Spectroscopy*, Opt. Lett. **43**, 939 (2018).
[25] C. Ferrante, E. Pontecorvo, G. Cerullo, M. H. Vos, and T. Scopigno, *Direct Observation of Subpicosecond Vibrational Dynamics in Photoexcited Myoglobin*, Nat. Chem. **8**, 1137 (2016).
[26] A. Kahan, O. Nahmias, N. Friedman, M. Sheves, and S. Ruhman, *Following Photoinduced Dynamics in Bacteriorhodopsin with 7-fs Impulsive Vibrational Spectroscopy*, J. Am. Chem. Soc. **129**, 537 (2007).
[27] M. Liebel, C. Schnedermann, T. Wende, and P. Kukura, *Principles and Applications of Broadband Impulsive Vibrational Spectroscopy*, J. Phys. Chem. A **119**, 9506 (2015).
[28] A. J. Musser, M. Liebel, C. Schnedermann, T. Wende, T. B. Kehoe, A. Rao, and P. Kukura, *Evidence for Conical Intersection Dynamics Mediating Ultrafast Singlet Exciton Fission*, Nat. Phys. **11**, 352 (2015).
[29] C. Schnedermann, M. Liebel, and P. Kukura, *Mode-Specificity of Vibrationally Coherent Internal Conversion in Rhodopsin During the Primary Visual Event*, J. Am. Chem. Soc. **137**, 2886 (2015).
[30] T. Wende, M. Liebel, C. Schnedermann, R. J. Pethick, and P. Kukura, *Population-Controlled Impulsive Vibrational Spectroscopy: Background- and Baseline-Free Raman Spectroscopy of Excited Electronic States*, J. Phys. Chem. A **118**, 9976 (2014).
[31] H. Kuramochi, S. Takeuchi, and T. Tahara, *Femtosecond Time-Resolved Impulsive Stimulated Raman Spectroscopy Using Sub-7-fs Pulses: Apparatus and Applications*, Rev. Sci. Instrum. **87**, 043107 (2016).
[32] H. Kuramochi, S. Takeuchi, K. Yonezawa, H. Kamikubo, M. Kataoka, and T. Tahara, *Probing the Early Stages of Photoreception in Photoactive Yellow Protein with Ultrafast Time-Domain Raman Spectroscopy*, Nat. Chem. **9**, 660 (2017).
[33] M. Maiuri, E. E. Ostroumov, R. G. Saer, R. E. Blankenship, and G. D. Scholes, *Coherent Wavepackets in the Fenna–Matthews–Olson Complex Are Robust to Excitonic-Structure Perturbations Caused by Mutagenesis*, Nat. Chem. **10**, 177 (2018).
[34] L. Monacelli, G. Batignani, G. Fumero, C. Ferrante, S. Mukamel, and T. Scopigno, *Manipulating Impulsive Stimulated Raman Spectroscopy with a Chirped Probe Pulse*, J. Phys. Chem. Lett. **8**, 966 (2017).
[35] G. Batignani, G. Fumero, A. R. S. Kandada, G. Cerullo, M. Gandini, C. Ferrante, A. Petrozza, and T. Scopigno, *Probing Femtosecond Lattice Displacement upon Photo-Carrier Generation in Lead Halide Perovskite*, Nat. Commun. **9**, 1971 (2018).
[36] G. Batignani, C. Ferrante, G. Fumero, and T. Scopigno, *Broadband Impulsive Stimulated Raman Scattering Based on a Chirped Detection*, J. Phys. Chem. Lett. **10**, 7789 (2019).
[37] P. Kukura, D. W. McCamant, and R. A. Mathies, *Femtosecond Stimulated Raman Spectroscopy*, Annu. Rev. Phys. Chem. **58**, 461 (2007).
[38] E. Pontecorvo, C. Ferrante, C. G. Elles, and T. Scopigno, *Spectrally Tailored Narrowband Pulses for Femtosecond Stimulated Raman Spectroscopy in the Range 330–750 nm*, Opt. Express **21**, 6866 (2013).
[39] Z. Piontkowski and D. W. McCamant, *Excited-State Planarization in Donor-Bridge Dye Sensitizers: Phenylene versus Thiophene Bridges*, J. Am. Chem. Soc. **140**, 11046 (2018).
[40] C. Ferrante, G. Batignani, G. Fumero, E. Pontecorvo, A. Virga, L. C. Montemiglio, G. Cerullo, M. H. Vos, and

T. Scopigno, *Resonant Broadband Stimulated Raman Scattering in Myoglobin*, J. Raman Spectrosc. **49**, 913 (2018).
[41] Y. Tanimura and S. Mukamel, *Two-Dimensional Femtosecond Vibrational Spectroscopy of Liquids*, J. Chem. Phys. **99**, 9496 (1993).
[42] A. Tokmakoff, M. J. Lang, D. S. Larsen, G. R. Fleming, V. Chernyak, and S. Mukamel, *Two-Dimensional Raman Spectroscopy of Vibrational Interactions in Liquids*, Phys. Rev. Lett. **79**, 2702 (1997).
[43] D. A. Blank, L. J. Kaufman, and G. R. Fleming, *Direct Fifth-Order Electronically Nonresonant Raman Scattering from* CS_2 *at Room Temperature*, J. Chem. Phys. **113**, 771 (2000).
[44] B. P. Molesky, Z. Guo, T. P. Cheshire, and A. M. Moran, *Perspective: Two-Dimensional Resonance Raman Spectroscopy*, J. Chem. Phys. **145**, 180901 (2016).
[45] Z. Guo, B. P. Molesky, T. P. Cheshire, and A. M. Moran, *Elucidation of Reactive Wavepackets by Two-Dimensional Resonance Raman Spectroscopy*, J. Chem. Phys. **143**, 124202 (2015).
[46] H. Frostig, T. Bayer, N. Dudovich, Y. C. Eldar, and Y. Silberberg, *Single-Beam Spectrally Controlled Two-Dimensional Raman Spectroscopy*, Nat. Photonics **9**, 339 (2015).
[47] S. Mukamel, D. Healion, Y. Zhang, and J. D. Biggs, *Multidimensional Attosecond Resonant X-Ray Spectroscopy of Molecules: Lessons from the Optical Regime*, Annu. Rev. Phys. Chem. **64**, 101 (2013).
[48] H. Kuramochi, S. Takeuchi, H. Kamikubo, M. Kataoka, and T. Tahara, *Fifth-Order Time-Domain Raman Spectroscopy of Photoactive Yellow Protein for Visualizing Vibrational Coupling in its Excited State*, Sci. Adv. **5**, eaau4490 (2019).
[49] T. Buckup and M. Motzkus, *Multidimensional Time-Resolved Spectroscopy of Vibrational Coherence in Biopolyenes*, Annu. Rev. Phys. Chem. **65**, 39 (2014).
[50] M. Cho, D. A. Blank, J. Sung, K. Park, S. Hahn, and G. R. Fleming, *Intrinsic Cascading Contributions to the Fifth- and Seventh-Order Electronically Off-Resonant Raman Spectroscopies*, J. Chem. Phys. **112**, 2082 (2000).
[51] K. C. Wilson, B. Lyons, R. Mehlenbacher, R. Sabatini, and D. W. McCamant, *Two-Dimensional Femtosecond Stimulated Raman Spectroscopy: Observation of Cascading Raman Signals in Acetonitrile*, J. Chem. Phys. **131**, 214502 (2009).
[52] R. Y. Tsien, *The Green Fluorescent Protein*, Annu. Rev. Biochem. **67**, 509 (1998).
[53] A. Acharya, A. M. Bogdanov, B. L. Grigorenko, K. B. Bravaya, A. V. Nemukhin, K. A. Lukyanov, and A. I. Krylov, *Photoinduced Chemistry in Fluorescent Proteins: Curse or Blessing?*, Chem. Rev. **117**, 758 (2017).
[54] See Supplemental Material at http://link.aps.org/supplemental/10.1103/PhysRevX.10.011051 for the 2D-ISRS time-time map (a); the 2D-ISRS maps averaged on different spectral probe regions (b); details on the derivation of the signal and the harmonic approximation (c and d); Liouville pathways for the reference simulations presented in the main text (e); details on the interpretation of spectral features in the 2D-ISRS spectra of GFP (f), and the effects of the Duschinsky angle on the relative intensities of fundamental and overtone transitions (g).
[55] We note that 2D Fourier-transformed spectra depend on positive and negative frequencies, as opposed to the 1D counterpart in which frequency axes of both signs carry the same information.
[56] D. A. Blank, L. J. Kaufman, and G. R. Fleming, *Fifth-Order Two-Dimensional Raman Spectra of* CS_2 *Are Dominated by Third-Order Cascades*, J. Chem. Phys. **111**, 3105 (1999).
[57] B. Dunlap, K. C. Wilson, and D. W. McCamant, *Phase-Matching and Dilution Effects in Two-Dimensional Femtosecond Stimulated Raman Spectroscopy*, J. Phys. Chem. A **117**, 6205 (2013).
[58] J. J. van Thor, *Photoreactions and Dynamics of the Green Fluorescent Protein*, Chem. Soc. Rev. **38**, 2935 (2009).
[59] M. Di Donato, L. J. G. W. van Wilderen, I. H. M. Van Stokkum, T. C. Stuart, J. T. M. Kennis, K. J. Hellingwerf, R. van Grondelle, and M. L. Groot, *Proton Transfer Events in GFP*, Phys. Chem. Chem. Phys. **13**, 16295 (2011).
[60] M. Chattoraj, B. A. King, G. U. Bublitz, and S. G. Boxer, *Ultra-Fast Excited State Dynamics in Green Fluorescent Protein: Multiple States and Proton Transfer*, Proc. Natl. Acad. Sci. U.S.A. **93**, 8362 (1996).
[61] C. Fang, R. R. Frontiera, R. Tran, and R. A. Mathies, *Mapping GFP Structure Evolution During Proton Transfer with Femtosecond Raman Spectroscopy*, Nature (London) **462**, 200 (2009).
[62] M. Kowalewski, B. P. Fingerhut, K. E. Dorfman, K. Bennett, and S. Mukamel, *Simulating Coherent Multidimensional Spectroscopy of Nonadiabatic Molecular Processes: From the Infrared to the X-Ray Regime*, Chem. Rev. **117**, 12165 (2017).
[63] S. Mukamel, *Principles of Nonlinear Optical Spectroscopy* (Oxford University, New York, 1999).
[64] K. E. Dorfman, B. P. Fingerhut, and S. Mukamel, *Broadband Infrared and Raman Probes of Excited-State Vibrational Molecular Dynamics: Simulation Protocols Based on Loop Diagrams*, Phys. Chem. Chem. Phys. **15**, 12348 (2013).
[65] G. Fumero, G. Batignani, K. E. Dorfman, S. Mukamel, and T. Scopigno, *On the Resolution Limit of Femtosecond Stimulated Raman Spectroscopy: Modelling Fifth-Order Signals with Overlapping Pulses*, ChemPhysChem **16**, 3438 (2015).
[66] S. Mukamel and J. D. Biggs, *Communication: Comment on the Effective Temporal and Spectral Resolution of Impulsive Stimulated Raman Signals*, J. Chem. Phys. **134**, 161101 (2011).
[67] F. Duschinsky, *The Importance of the Electron Spectrum in Multi Atomic Molecules. Concerning the Franck-Condon Principle*, Acta Physicochim. URSS **7**, 551 (1937).
[68] H. Kupka and P. H. Cribb, *Multidimensional Franck–Condon integrals and Duschinsky mixing effects*, J. Chem. Phys. **85**, 1303 (1986).
[69] R. Gnanasekaran, *Normal Modes and the Duschinsky Mixing of the Ground- and Excited-State Vibrations of the Green Fluorescent Protein Chromophore*, Chem. Phys. Lett. **587**, 61 (2013).
[70] G. M. Sando, K. G. Spears, J. T. Hupp, and P. T. Ruhoff, *Large Electron Transfer Rate Effects from the Duschinsky Mixing of Vibrations*, J. Phys. Chem. A **105**, 5317 (2001).

[71] G. Tian, S. Duan, G.-P. Zhang, W. Hu, and Y. Luo, *The Effect of Duschinsky Rotation on Charge Transport Properties of Molecular Junctions in the Sequential Tunneling Regime*, Phys. Chem. Chem. Phys. **17**, 23007 (2015).

[72] B. Salna, A. Benabbas, J. T. Sage, J. van Thor, and P. M. Champion, *Wide-Dynamic-Range Kinetic Investigations of Deep Proton Tunnelling in Proteins*, Nat. Chem. **8**, 874 (2016).

[73] J. T. S. Hopper *et al.*, *Detergent-Free Mass Spectrometry of Membrane Protein Complexes*, Nat. Methods **10**, 1206 (2013).

[74] M. Liebel, C. Schnedermann, and P. Kukura, *Sub-10-fs Pulses Tunable from 480 to 980 nm from a NOPA Pumped by an Yb: KGW Source*, Opt. Lett. **39**, 4112 (2014).

[75] G. Batignani, G. Fumero, E. Pontecorvo, C. Ferrante, S. Mukamel, and T. Scopigno, *Genuine Dynamics vs Cross Phase Modulation Artifacts in Femtosecond Stimulated Raman Spectroscopy*, ACS Photonics **6**, 492 (2019).

[76] G. Batignani, E. Pontecorvo, D. Bossini, C. Ferrante, G. Fumero, G. Cerullo, S. Mukamel, and T. Scopigno, *Modeling the Ultrafast Response of Two-Magnon Raman Excitations in Antiferromagnets on the Femtosecond Timescale*, Ann. Phys. (N.Y.) **531**, 1900439 (2019).

Supplemental Material: Two-dimensional impulsively stimulated resonant Raman spectroscopy of molecular excited-states

Giuseppe Fumero[1,2],* Christoph Schnedermann[3,4],* Giovanni Batignani[1], Torsten Wende[3], Matz Liebel[3,5], Giovanni Bassolino[3], Carino Ferrante[1,6], Shaul Mukamel[7], Philipp Kukura[3],† and Tullio Scopigno[1,6]‡

[1] *Dipartimento di Fisica, Sapienza Universitá di Roma, Piazzale Aldo Moro 5, Roma, I-00185, Italy*

[2] *Dipartimento di Scienze di Base e Applicate per l'Ingegneria, Sapienza Universitá di Roma, Via Antonio Scarpa 14/16, Roma, I-00161, Italy*

[3] *Physical and Theoretical Chemistry Laboratory, South Parks Road, Oxford, OX1 3QZ, United Kingdom*

[4] *Cavendish Laboratory, Department of Physics, University of Cambridge, Cambridge, CB3 0HE, UK*

[5] *ICFO -Institut de Ciencies Fotoniques, The Barcelona Institute of Science and Technology, Barcelona, 08860 Castelldefels, Spain*

[6] *Istituto Italiano di Tecnologia, Center for Life Nano Science @Sapienza, Roma, I-00161, Italy and*

[7] *Department of Chemistry, University of California, Irvine, 92623, California*

(Dated: January 14, 2020)

a. 2D-ISRS time-time map

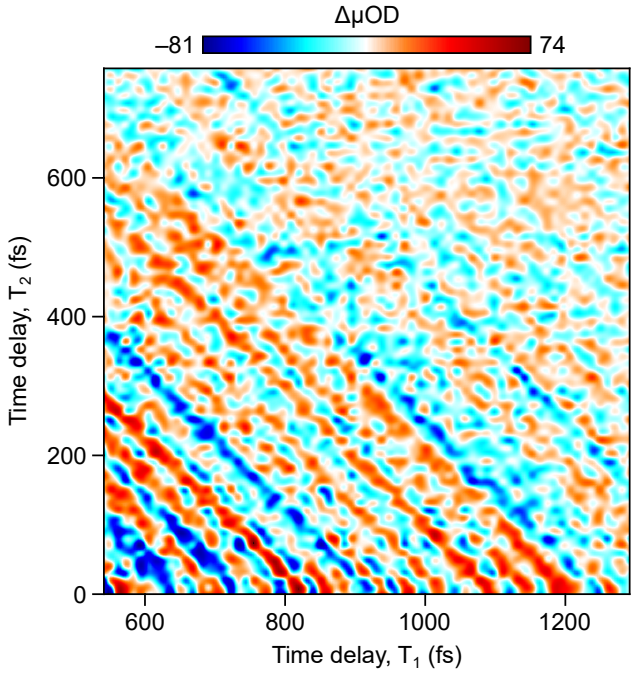

FIG. S1: 2D-ISRS time-time map $S(T_1, T_2)$ obtained by extracting the oscillatory part of the detected signal at each probe wavelength along T_2 for every recorded time point along T_1. The frequency domain map $S(\Omega_1, \Omega_2)$ (shown in Fig. 3 of the main text) has been obtained from this map by 2D Fourier transforming and averaging over the probe spectral region resonant with the stimulated emission as detailed in the main text.

b. Selective resonance contributions by averaging on different spectral probe regions

Resonant 2D-ISRS can be used to correlate the changes of the coordinate displacements to the resonant conditions of the probe pulse and understand how the multidimensional energy landscape of the sample is modified by dynamics on different potential energy surfaces, by averaging the broadband probe in different spectral regions. In Fig. S2, we show the 2D maps averaged in the stimulated emission (SE), between 520 and 680 nm, and in the excited-state absorption (ESA), between 620 and 680 nm. The ESA band displays a more shallow transient absorption spectrum compared to the SE region (Fig. 2(b), main text), which resulted in a lower overall signal to noise ratio, preventing a thorough quantitative analysis. Nevertheless, we can observe that the distribution of diagonal and off-diagonal peaks is different in the two cases.

* Authors contributed equally.
† philipp.kukura@chem.ox.ac.uk
‡ tullio.scopigno@uniroma1.it

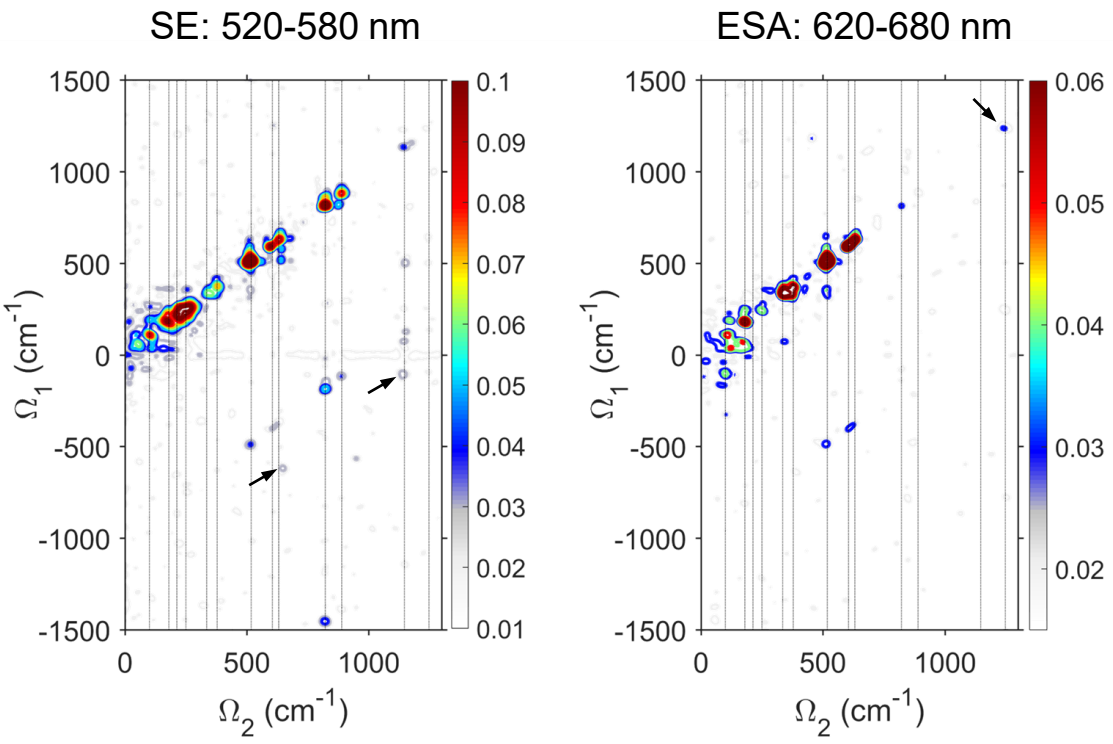

FIG. S2: 2D-ISRS map of GFP for different resonance conditions of the probe pulse. The left and right panels have been obtained averaging the spectrally resolved maps over the spectral region corresponding to the SE and ESA, respectively. The black arrows highlight the combination band of the 1248 cm^{-1} in the SE configuration and the corresponding diagonal peak at 1248 cm^{-1} in the ESA configuration.

The enhancement or suppression of certain peaks in the maps detected with the ESA and SE probing windows is a consequence of the different displacements d_3 involved, which makes 2D-ISRS highly versatile in elucidating different aspects of the potential energy landscape. In particular, a stronger diagonal peak at 1248 cm^{-1} in the ESA configuration reveals a larger displacement d_3 of the 1248 cm^{-1} mode. This is in agreement with the presence of the combination peaks involving the 1248 cm^{-1} mode in the SE resonant map, since in the ESA configuration d_3 is the displacement between S_1 and S_n, corresponding to d_2 in the SE configuration.

In the ESA configuration, the peaks involving the modes at 822, 890 and 1147 cm^{-1} are significantly suppressed compared to the SE map, as shown by the principal diagonal in the right panel of Fig. S2, pointing to a lower value of the displacements d_3 along these vibrational coordinates. Since both a combination peak at ($\Omega_1 = \omega_j \pm \omega_i$, $\Omega_2 = \omega_j$) and a cross peak at ($\Omega_1 = \pm\omega_i$, $\Omega_2 = \omega_j$) requires a non-vanishing d_3 along ω_j (see the right panel of Fig. 4(c) in the main text and section

f of this SM), a lower value of the displacement d_3 justifies the suppression of all the off-diagonal peaks laying on vertical strips at frequencies corresponding to these modes.

We remark that the detection in the ESA region may also reveal different processes with respect to the SE analogue, due to possible additional pathways that involve the creation of vibrational coherences on S_n by the Raman pulse. These pathways are resonantly suppressed by the SE detection but can still contribute in the ESA configuration.

c. Derivation of the signal

We consider, as a reference model, the same three electronic level system with a ground and two excited electronic states, S_0, S_1 and S_n, considered in the main text, with the associated vibrational manifolds. 2D-ISRS process is described by the Hamiltonian

$$H = H_0 + H' \tag{S1}$$

where H_0 is the free molecule and H' is the interaction term. In the dipole approximation, H' is the Power-Zienau radiation-matter interaction Hamiltonian [1]

$$H'(t) = V \cdot \mathcal{E}^*(t) + c.c. \tag{S2}$$

where V is the dipole operator and $\mathcal{E}$ the positive frequency component of the total field

$$E(\mathbf{r}, t) = \sum_j \mathcal{E}_j(t - T_j) e^{i\mathbf{k_j}\cdot\mathbf{r}} + c.c. \tag{S3}$$

The summation runs over the spectral modes of the field which consists in the three delayed pulses used in the experiment: an actinic femtosecond pump $\mathcal{E}_a$ resonant with the ground-state absorption S_0-S_1, a femtosecond Raman pulse $\mathcal{E}_p$, resonant with the excited-state absorption S_1-S_n and a broadband continuum probe $\mathcal{E}_s$, resonant with the stimulated emission from S_1. The detection protocol consists of the spectral dispersion of a broadband probe pulse resonant with the stimulated emission from S_1 (see Fig. 2(b) of the main text), after the interaction with the sample, previously excited by the actinic and Raman pulses. We consider well separated pulses, with delays T_1, between the $\mathcal{E}_a$ and $\mathcal{E}_p$, and T_2, between $\mathcal{E}_p$ and $\mathcal{E}_s$, greater than the pulses temporal envelopes. In the frequency-dispersed heterodyne detection, the signal is given by the interferometric transmission of the field $\mathcal{E}_S$, which acts as a local oscillator [2]:

$$S(\omega, T_1, T_2) = \mathbf{Im}\ \mathcal{E}_s^*(\omega) P(\omega, T_1, T_2) = \mathbf{Im}\ \mathcal{E}_s^*(\omega) \int_{-\infty}^{+\infty} dt\, e^{i\omega t}\, \mathrm{Tr}\left[V e^{-\frac{i}{\hbar}\int_{-\infty}^{t} dt'\, H'_-(t', T_1, T_2)} \rho(-\infty) \right] \tag{S4}$$

$P(t) = \langle V(t) \rangle = \mathrm{Tr}[V\rho(t)]$ represents the nonlinear polarization induced by the interactions and the Liouville superoperator $H'_- = [H', \cdot]$ acts on the equilibrium density matrix $\rho(-\infty)$ in the interaction picture. The 2D-ISRS signal is obtained expanding the exponential in Eq. S4 to the fifth order in radiation-matter interaction and the expression depends on the delays T_1 and T_2 and on the dispersed frequency ω. Each of the term arising from the commutators brought by H' in the expansion can be represented by a Feynman diagram, which facilitates the calculation of the signal.

The total polarization in Eq. S4 is obtained by the sum of the four diagrams $i - iv$ that contribute to the process, shown in Fig. S3(a). Equivalently, since the heterodyne detection is sensitive to the imaginary part of the signal, their complex conjugates shown in Fig. S3(b) can be used. However, to speed up the calculation, it is convenient to derive the signal summing either odd or even numbered diagrams in Fig. S3, as shown in the following. The vertical lines of the diagrams represent the evolution in time of the ket and bra sides of the density matrix, time going from the bottom to the top. The arrows represent interactions with the electromagnetic field. The first five interactions with the external pulses prepare the system in a non-equilibrium state, and an additional light matter interaction (represented by the wavy arrow) allows for relaxation through the emission of the signal and is typically referred as the free induction decay. Since the signal in Eq. S4 is proportional to the trace, a non-vanishing signal requires a diagonal density matrix after the action of the free induction decay. Reading off the diagrams, we obtain:

$$S^{(5)}(\omega, T_1, T_2) = \mathbf{Im}\left[\left(-\frac{i}{\hbar}\right)^5 \int_{-\infty}^{\infty} dt e^{i\omega t} \mathcal{E}_s^*(\omega) \int_{-\infty}^{t}\int_{-\infty}^{t_5}\int_{-\infty}^{t_4}\int_{-\infty}^{t_3}\int_{-\infty}^{t_2} dt_5 \dots dt_1 \, \mathcal{E}_a(t_1)\mathcal{E}_a^*(t_2) \right.$$
$$\left. \mathcal{E}_p(t_3 - T_1)\mathcal{E}_p^*(t_4 - T_1)\mathcal{E}_s(t_5 - T_2 - T_1)\, \mathcal{F}(t, t_1, t_2, t_3, t_4, t_5)\right]$$

The matter correlation function $\mathcal{F}$ is derived from the Feynman paths $i - iv$ in Fig. S3:

$$\mathcal{F} = [F_i + F_{ii} + F_{iii} + F_{iv}] \tag{S5}$$

where

$$F_i = \left\langle VG(t - t_5)V^\dagger G(t_5 - t_4)VG(t_4 - t_3)V^\dagger G(t_3 - t_2)VG(t_2 - t_1)V^\dagger \right\rangle \tag{S6a}$$
$$F_{ii} = \left\langle VG(t - t_5)V^\dagger G(t_5 - t_4)V^\dagger G(t_4 - t_3)VG(t_3 - t_2)VG(t_2 - t_1)V^\dagger \right\rangle \tag{S6b}$$
$$F_{iii} = \left\langle VG(t - t_5)V^\dagger G(t_5 - t_4)VG(t_4 - t_3)V^\dagger G(t_3 - t_2)V^\dagger G(t_2 - t_1)V \right\rangle \tag{S6c}$$
$$F_{iv} = \left\langle VG(t - t_5)V^\dagger G(t_5 - t_4)V^\dagger G(t_4 - t_3)VG(t_3 - t_2)V^\dagger G(t_2 - t_1)V \right\rangle \tag{S6d}$$

where V is the dipole operator (with dipole matrix elements μ_{ij}) and G is the retarded Green function in time domain

$$G(t'-t'') = \theta(t'-t'')e^{-iH_0(t'-t'')} \tag{S7}$$

Similarly, signal expressions for diagrams $v-viii$ of Fig. S3(b) can be obtained. In this case, since the last interaction is an absorption, the heterodyne-detected signal is the complex conjugate of Eq. S4:

$$S^{(5)}(\omega,T_1,T_2) = -\mathbf{Im}\ \mathcal{E}_s(\omega)P^{(5)}(-\omega,T_1,T_2) = -\mathbf{Im}\int e^{-i\omega t}\mathcal{E}_s(\omega)P^{(5)}(t,T_1,T_2) \tag{S8}$$

and the related correlation functions read:

$$F_v = \left\langle V^\dagger G(t-t_5)VG(t_5-t_4)VG(t_4-t_3)V^\dagger G(t_3-t_2)VG(t_2-t_1)V^\dagger \right\rangle \tag{S9a}$$

$$F_{vi} = \left\langle V^\dagger G(t-t_5)VG(t_5-t_4)V^\dagger G(t_4-t_3)VG(t_3-t_2)VG(t_2-t_1)V^\dagger \right\rangle \tag{S9b}$$

$$F_{vii} = \left\langle V^\dagger G(t-t_5)VG(t_5-t_4)VG(t_4-t_3)V^\dagger G(t_3-t_2)V^\dagger G(t_2-t_1)V \right\rangle \tag{S9c}$$

$$F_{viii} = \left\langle V^\dagger G(t-t_5)VG(t_5-t_4)V^\dagger G(t_4-t_3)VG(t_3-t_2)V^\dagger G(t_2-t_1)V \right\rangle \tag{S9d}$$

The brakets in the expressions S6 and S9 can be solved expanding the signal as a sum-over-states (SoS) corresponding to the eigenfunctions of H_0. Since the pulses are well separated, it is possible to extend the integration over t_2 and t_4 to $+\infty$, obtaining two delta functions that can be used to break up the multiple integration. The total signal can be thus expressed as

$$S^{(5)}(\omega,T_1,T_2) = S^{(5)}_{odd}(\omega,T_1,T_2) + S^{(5)}_{even}(\omega,T_1,T_2) \tag{S10}$$

where in $S^{(5)}_{odd}$ and $S^{(5)}_{even}$ we gathered the contributions from even and odd numbered diagrams of Fig. S3:

$$S^{(5)}_{odd}(\omega,T_1,T_2) = \sum_{\substack{g,g',f\\e,e',e''}} K(g)\,\mathbf{Im}\left\{\left[\frac{\mu_{g'e''}\mu^*_{g'e'}\,\mathcal{E}^*_s(\omega)\,\mathcal{E}_s(\omega-\omega_{e''e'})}{2(\omega-\tilde{\omega}_{e''g'})} - \frac{\mu_{g'e''}\mu^*_{e'g'}\,\mathcal{E}_s(\omega)\,\mathcal{E}^*_s(\omega+\omega_{e''e'})}{2(\omega+\tilde{\omega}_{g'e'})}\right] e^{-i\,\tilde{\omega}_{ee'}T_1}\right.$$
$$\left. e^{-i\,\tilde{\omega}_{e''e'}T_2}\,\mu_{e''f}\mu^*_{fe}\,\mathcal{W}_p(\omega_{e''e'}-\omega_{ee'},\tilde{\omega}_{e''e'}-\tilde{\omega}_{fe'})\,\mu_{e'g}\mu^*_{eg}\,\left[\mathcal{W}_a(\omega_{ee'},\tilde{\omega}_{ee'}-\tilde{\omega}_{eg})-\mathcal{W}_a(\omega_{ee'},\tilde{\omega}_{ge'})\right]\right\} \tag{S11}$$

$$S^{(5)}_{even}(\omega,T_1,T_2) = \sum_{\substack{g,g',f\\e,e',e''}} K(g)\,\mathbf{Im}\left\{\left[\frac{\mu_{g'e}\mu^*_{g'e''}\,\mathcal{E}^*_s(\omega)\,\mathcal{E}_s(\omega-\omega_{ee''})}{2(\omega-\tilde{\omega}_{eg'})} - \frac{\mu^*_{e''g'}\mu_{g'e}\,\mathcal{E}_s(\omega)\,\mathcal{E}^*_s(\omega+\omega_{ee''})}{2(\omega+\tilde{\omega}_{g'e''})}\right] e^{-i\,\tilde{\omega}_{ee'}T_1}\right.$$
$$\left. e^{-i\,\tilde{\omega}_{ee''}T_2}\,\mu_{fe'}\mu^*_{e''f}\,\mathcal{W}_p(\omega_{ee''}-\omega_{ee'},-\tilde{\omega}_{ee'}+\tilde{\omega}_{ef})\,\mu_{e'g}\mu^*_{eg}\,\left[\mathcal{W}_a(\omega_{ee'},\tilde{\omega}_{ee'}-\tilde{\omega}_{eg})-\mathcal{W}_a(\omega_{ee'},\tilde{\omega}_{ge'})\right]\right\} \tag{S12}$$

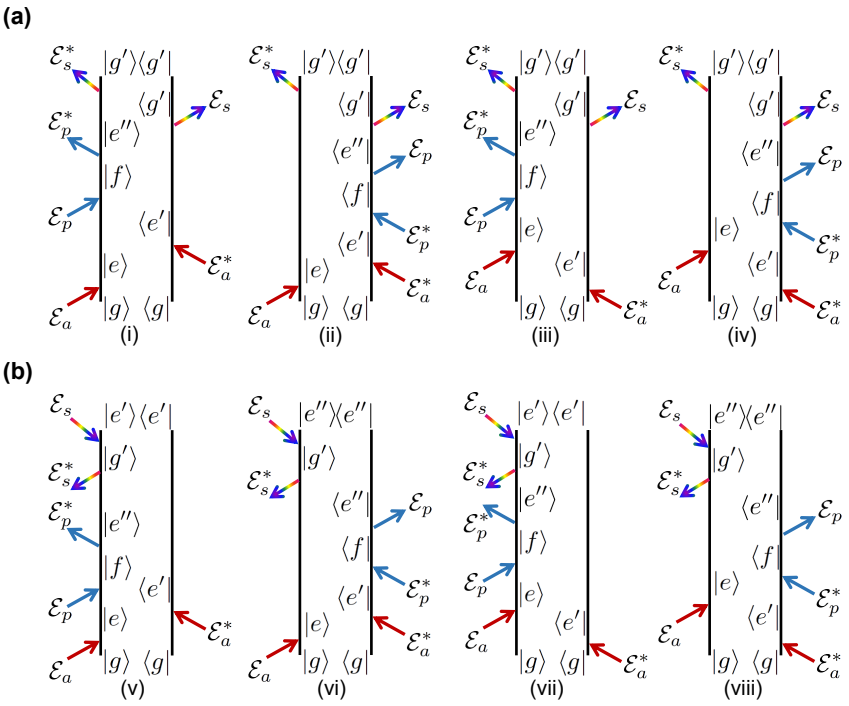

FIG. S3: Double sided Feynman diagrams contributing to the 2D-ISRS signal averaged in the SE region of the probe pulse.

where the weighted pulse spectral densities $\mathcal{W}_k(\omega_1, \tilde{\omega}_2)$ and the indexes of the summation are those defined in the main text and $K(g)$ is the Boltzman factor. These expressions are equivalent and correspond to the summation of diagrams $i - iv$, with the advantage of having only one integral of the weighted pulse spectral density of the pulse $\mathcal{E}_p$ that has to be calculated. A Fourier transformation over the two delays and the integration on ω lead to the 2D frequency correlation map:

$$S^{(5)}(\Omega_1, \Omega_2) = \int_{-\infty}^{+\infty} d\omega \int_{-\infty}^{+\infty} dT_1 dT_2 e^{i\Omega_1 T_1 + i\Omega_2 T_2} S^{(5)}(\omega, T_1, T_2) \tag{S13}$$

We note that, for each combination of the dummy SoS indexes in Eq. S11 and S12, each diagram contributes to the signal via a product of two weighted pulse spectral densities, ruled by the spectral widths of the actinic and Raman pulse, a function of ω, related to the transition induced by the probe pulse and a complex exponential function of the delays T_1 and T_2 that selects the position of the associated peak in the 2D spectrum. Thus, in the SoS picture, the signal is determined by contributions of different pathways in the Liouville space, corresponding to the different permutation of the SoS indexes.

d. Harmonic approximation

In the harmonic approximation, the vibrational manifold associated with each electronic state can be depicted as an n-dimensional parabola, where n is the number of normal modes of the sample. H_0 is then given by a collection of harmonic oscillators (HO):

$$H_0 = \sum_{j=0}^{2} = H_{S_j}^{HO} \quad \text{with} \;\; H_{S_j}^{HO} = \sum_{\nu_j} \frac{m\dot{Q}_{\nu_j}^2}{2} + \frac{m\omega_{\nu_j}(Q_{\nu_j} + d_{\nu_j})^2}{2} \tag{S14}$$

where ν_j runs over the vibrational manifold of S_j, while Q_{ν_j} and d_{ν_j} are the corresponding mass-weighted normal coordinate and displacement. Within the Born-Oppenheimer approximation, the dipole matrix elements read relative to the vibronic transition $\{S, \nu\} \rightarrow \{S', \nu'\}$ reads

$$\mu_{S\nu;S'\,\nu'} = \langle \nu'(Q') |\, \mu_{S';S}(Q)\, | \nu(Q) \rangle \tag{S15}$$

where S, ν, Q are the initial electronic state, vibrational eigenfunction and normal mode coordinate involved in the transition, with their corresponding primed analogues relative to the final state, and $\mu_{S';S}$ is the electronic transition dipole. Since an analytical expression for $\mu_{S';S}(Q)$ is generally not available, the electronic dipole is usually expanded in Taylor series of Q_i around the initial state equilibrium geometry, described by the coordinates Q_{0i}

$$\mu_{S';S}(Q) = \mu_{S';S}(Q_0) + \sum_i \frac{\partial \mu_{S';S}}{\partial Q_i}(Q_i - Q_{0i}) + \mathcal{O}(Q^2) \tag{S16}$$

In this work we assumed the Condon approximation [3], in which only the constant 0^{th} order term is retained, obtaining $\mu_{S';S}(Q) \approx \mu_{S';S}(Q_0)$. Since this term does not depend on the vibrational state, it is the same for all the pathways in Eqs. (S12)-(S11) and we included it simply as common multiplying factor. The extension to the Herzberg-Teller and nonlinear corrections can be easily accounted for in the model including in the calculation the higher order terms in $\mu_{S';S}$ [4, 5].
Consequently, the relative intensities of different features in the 2D-ISRS spectra are ruled by the Franck-Condon (FC) factors $\mu_{\nu',\nu} = \langle \nu'(Q') | \nu(Q) \rangle$ that account for the overlap of ground and excited state vibrational wavefunctions. Since many modes populate a typical vibration manifold, the resulting wavefunction exists in a multidimensional landscape. Consequently, calculating FC factors requires a multidimensional integration, whose calculation is complicated by mode-mixing in the excited state, namely the Duschinsky rotation, and by changes in the vibrational frequencies. The Duschinsky effect [6] arises when two electronic states possess different equilibrium geometries and hence the corresponding normal modes are nonparallel. In this case

$$Q' = JQ + D \tag{S17}$$

where J is the orthogonal Duschinsky matrix and D is the vector of displacements and

$$\langle \nu | \nu' \rangle = \int_{-\infty}^{\infty} dQ\, dQ'\ \psi_{\nu}(Q)\psi_{\nu'}(Q') \tag{S18}$$

being ψ_ν the HO eigenfunction

$$\psi_{\nu}(Q) = \prod_i (\frac{\sqrt{\frac{\omega_i}{\hbar}} 2^{\nu_i}}{\nu_i! \sqrt{\pi}})^{\frac{1}{2}} H_{\nu_i}(Q_i) e^{-\frac{1}{2}\frac{\omega_i}{\hbar}Q_i^2} \tag{S19}$$

Considering pairs of modes, these effects can be visualized as a displacement and a rotation between the associated two-dimensional PES of the initial and final electronic states. If $J = \mathbb{I}$ is the identity operator, the total wavefunction is the product of uncorrelated single mode linearly displaced harmonic oscillators (LDHO), whose excited-state PES are displaced along the normal mode coordinates with respect to the ground-state potential. The FC factors in the linearly displaced harmonic oscillator (LDHO) are simply calculated by the overlap of the single mode wavefunctions:

$$\langle \nu | \nu' \rangle = \prod_{i,j} \langle \nu_i | \nu'_j \rangle \tag{S20}$$

e. Liouville pathways for reference simulations

The following reference pathways show the origin of the peaks reported in the simulations of Fig. 4 in the main text:

$$|00\rangle\langle 00| \rightarrow |01\rangle\langle 00| \rightarrow |01\rangle\langle 00| \rightarrow |00\rangle\langle 00| \tag{S21a}$$

$$|00\rangle\langle 00| \rightarrow |11\rangle\langle 00| \rightarrow |01\rangle\langle 00| \rightarrow |00\rangle\langle 00| \tag{S21b}$$

$$|00\rangle\langle 00| \rightarrow |01\rangle\langle 01| \rightarrow |01\rangle\langle 00| \rightarrow |00\rangle\langle 00| \tag{S21c}$$

$$|00\rangle\langle 00| \rightarrow |01\rangle\langle 00| \rightarrow |10\rangle\langle 00| \rightarrow |00\rangle\langle 00| \tag{S21d}$$

where $|ab\rangle\langle ba|$ represent the state of the density matrix with the corresponding occupational number for modes ω_a and ω_b and each arrow is the interaction with a field. These pathways offer an overview of the origin of the peaks in 2D-ISRS maps: Eq. S21a correspond to a diagonal peak at ω_a, Eq. S21b-c to combination peaks at the sum and difference frequencies along Ω_1, and Eq. S21d to a cross peak with $\Omega_1 = \omega_a$ and $\Omega_2 = \omega_b$.

f. Details on the interpretation of spectral features in the 2D-ISRS spectra of GFP

Following the nomenclature used in the main text, off-diagonal peaks in the 2D-ISRS spectra of GFP can be classified as cross and combination peaks, depending on the associated Liouville

pathway which determines their position in the two-dimensional map. A cross peak is a feature at ($\Omega_1 = \pm\omega_i$, $\Omega_2 = \omega_j$), which implies a vibrational coherence on ω_i during T_1 and ω_j during T_2 (with $i \neq j$). On the contrary, a combination peak appears at ($\Omega_1 = \omega_j \pm \omega_i$, $\Omega_2 = \omega_j$) in the 2D-ISRS map and is generated by pathways where the density matrix oscillates with frequency $\omega_j \pm \omega_j$ during T_1 and ω_j during T_2. The origin of the peak in the 2D-ISRS map can be obtained from the fitted spectrum presented in Fig. 3 (b) of the main text. The position and intensity of the fitted peaks are ruled by the displacements relative to the modes from which the peaks originates, as detailed by the conditions presented in the main text. For example, the following considerations can be made regarding the presence or absence of specific features in the 2D-ISRS map related to the two modes at frequencies 605 and 1010 cm^{-1}:

- The peak at ($\Omega_1 = 605 cm^{-1}$, $\Omega_2 = 605 cm^{-1}$) is the diagonal peak generated by the 605 cm^{-1} normal mode, which originates from a coherence on such mode during both T_1 and T_2 and requires $d_1^{605} \neq 0$ and $d_3^{605} \neq 0$;

- The diagonal peak at ($\Omega_1 = 1010 cm^{-1}$, $\Omega_2 = 1010 cm^{-1}$), involving the fundamental of the 1010 cm^{-1} mode, does not appear in the 2D map, due to a weak displacement d_3^{1010};

- The peak at ($\Omega_1 = -405 cm^{-1}$, $\Omega_2 = 605 cm^{-1}$) is a combination peak between the modes at 605 cm^{-1} and 1010 cm^{-1} and results from non-vanishing d_1^{605}, d_1^{1010}, d_2^{1010} and d_3^{605}.

- The cross peak at ($\Omega_1 = 1010 cm^{-1}$, $\Omega_2 = 605 cm^{-1}$) does not appear in the 2D map since d_2^{605} is weak.

- The anti-diagonal peaks at ($\Omega_1 = -605 cm^{-1}$, $\Omega_2 = 605 cm^{-1}$) and ($\Omega_1 = -1010 cm^{-1}$, $\Omega_2 = 1010 cm^{-1}$) do not appear in the 2D map, since d_2^{605} and d_3^{1010} are weak, respectively.

Anti-diagonal peaks located at ($\Omega_1 = -\omega_i, \Omega_2 = \omega_i$) in the 2D spectra are a particular class of off-diagonal features. They involve the generation of a coherence on the same mode, oscillating at ω_i during both T_1 and T_2. These features can originate both from a cross peak of the mode with itself or from a combination band with the overtone of the fundamental, as represented by the pathways

$$|00\rangle\langle 00| \rightarrow |01\rangle\langle 00| \rightarrow |00\rangle\langle 10| \rightarrow |00\rangle\langle 00| \tag{S22a}$$

$$|00\rangle\langle 00| \rightarrow |01\rangle\langle 00| \rightarrow |01\rangle\langle 20| \rightarrow |01\rangle\langle 10| \tag{S22b}$$

We remark that these signals are expected to be generally weak, since they would require a large displacement d_2, able by instance to couples the fundamental frequency and its overtone, together with

non-negligible displacements d_1 and d_3. In the GFP, we observe it only for the 1147 cm^{-1} mode, which shows prominent couplings with its overtone. In table I, we summarize the features obtained in the 2D-ISRS fitted spectrum shown in Fig. 3(b) of the main text. The fundamental frequencies corresponding to the modes considered in the model are reported in the first row and column of the table. We have used the following shortened notation to indicate the origin and position of the peaks in the table:

$$\mathrm{D}(\omega_i) = (\Omega_1 = \omega_i, \Omega_2 = \omega_i)$$
$$\mathrm{X}_{\pm}(\omega_i, \omega_j) = (\Omega_1 = \pm\omega_i, \Omega_2 = \omega_j)$$
$$\mathrm{C}_{\pm}(\omega_i, \omega_j) = (\Omega_1 = \omega_j \pm \omega_i, \Omega_2 = \omega_j)$$
$$\mathrm{OC}_{\pm}(\omega_i, \omega_j) = (\Omega_1 = \omega_j \pm 2\omega_i, \Omega_2 = \omega_j)$$

For example, the notation C_- in the first column, eighth row of the table indicate a combination peak at ($\Omega_1 = 102 - 1147\,\mathrm{cm}^{-1}$, $\Omega_2 = 102\,\mathrm{cm}^{-1}$). Bold symbols indicate off-diagonal peaks obtained with the addition of the Duschinsky mixing to the model.

ω_i \ ω_j	102	190	337	517	605	822	888	1010	1147	1248
102	D								$\mathrm{C}_{\pm}$,$\mathrm{X}_{\pm}$	
190		D							X_{+}	
337			D	X_{+}						
517				D					$\mathrm{X}_{\pm}$	
605					D					
822						D	X_{+}			
888							D			
1010	C_-,X_-		C_-	$\mathrm{C}_{\pm}$	$\mathrm{C}_{\pm}$	C_-	C_-		X_{+}	
1147							**OC_-**	**OC_-**	D, X_-, **OC_-**	
1248				C_-	C_-	C_-	C_-		X_{+},C_-	D

TABLE I: Origin of the peaks in the fitted 2D-ISRS spectrum shown in Fig. 3(a) of the main text.

We note that a combination feature of the type X_+ will appear at higher Ω_1 with respect to the corresponding cross peak involving the same modes, because the density matrix during T_1 oscillates at the sum of the fundamental frequencies. This reflects in an asymmetry between the number of combination peaks at positive and negative Ω_1, since peaks involving high frequency modes may lay outside the sampled region of the 2D spectra. In general, both cross and combination peaks can appear at positive and negative frequencies for the first coherence, depending on the frequencies involved. On the contrary, only positive values of Ω_2 are shown in the 2D spectra because of the inversion symmetry of the 2D Fourier transform.

g. Effects of the Duschinsky angle on the relative intensities of fundamental and overtone transitions

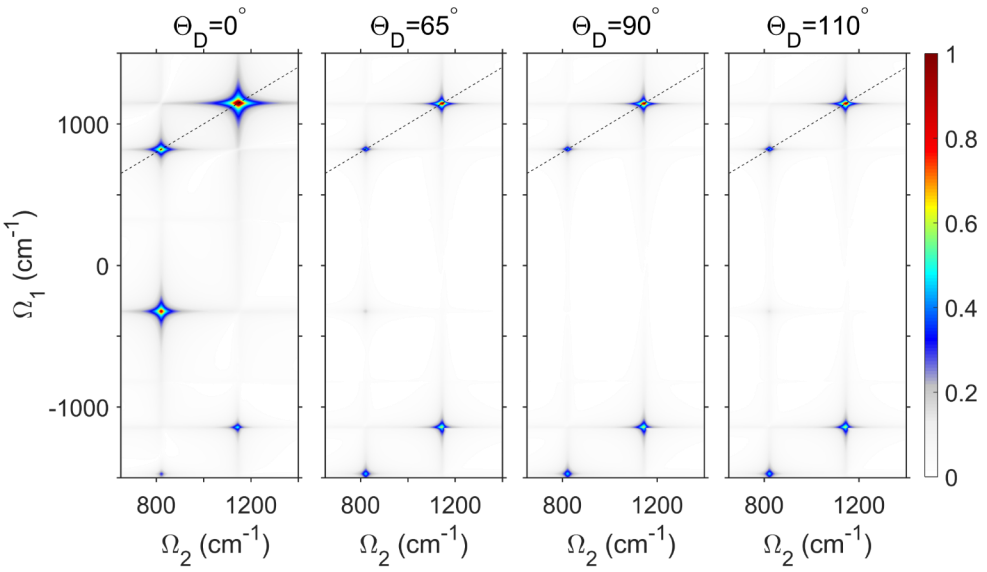

FIG. S4: Effect of mode mixing on the 2D-ISRS maps. Simulations of the 2D-ISRS signal for the system presented in Fig. 5 of the main text, with two modes at frequencies 822 and 1147 cm^{-1} coupled to a non-displaced low-frequency mode at 80 cm^{-1}. The Duschinsky angle between projections of the excited states S_1 and S_n along the 1147 and 80 cm^{-1} modes is varied from 0° in the left panel to 110° in the right panel. A finite Duschinsky angle leads to the suppression of the sub-diagonal peak at the fundamental frequency $\Omega_1 = \Omega_2 - 1147$ cm^{-1} and enhances the intensity of the overtone couplings, as shown by the simulations with $\Theta_D = 65^\circ$, 90° and 110°.

As discussed in the main text, Duschinsky mixing affects the relative intensities of fundamental and overtone contributions to the off-diagonal peaks in the 2D map. In particular, in figure S4, we evaluated the effect of different Duschinsky angles on the combination bands in the model system with three vibrational modes at 822, 1147 and 80 cm^{-1} considered in the main text. The combination band between the modes at 822 and 1147 cm^{-1}, dominant in the absence of mixing, is suppressed for Θ_D ranging between 65°-110°, while the intensity of the coupling of the 822 cm^{-1} to the overtone at $2294 = 2 \cdot 1147$ cm^{-1} is enhanced.

[1] E. A. Power and S. Zienau, Coulomb Gauge in Non-Relativistic Quantum Electro-Dynamics and the Shape of Spectral Lines, Phil. Trans. R. Soc. A **251**, 427 (1959).

[2] S. Mukamel, Principles of Nonlinear Optical Spectroscopy, Oxford University Press, 1999.

[3] E.U. Condon, The Franck-Condon Principle and Related Topics, Am. J.Phys. **15**, 365 (1947).

[4] G. Herzberg and E. Teller, Schwingungsstruktur der Elektronenübergänge bei mehratomigen Molekülen, Z. Phys. Chem. 21B (1933).

[5] M. Dierksen and S. Grimme, Density functional calculations of the vibronic structure of electronic absorption spectra, J. Chem. Phys. **120**, 3544 (2004).

[6] F. Duschinsky, The importance of the electron spectrum in multi atomic molecules. Concerning the Franck-Condon principle, Acta Physicochim. URSS **7**, 551–566 (1937).